A preliminary sizing method for hybrid-electric aircraft including aero-propulsive interaction effects

de Vries, Reynard; Brown, Malcom T.; Vos, Roelof

DOI
10.2514/6.2018-4228

Publication date
2018

Document Version
Accepted author manuscript

Published in
2018 Aviation Technology, Integration, and Operations Conference

Citation (APA)
de Vries, R., Brown, M. T., & Vos, R. (2018). A preliminary sizing method for hybrid-electric aircraft including aero-propulsive interaction effects. In *2018 Aviation Technology, Integration, and Operations Conference* Article AIAA 2018-4228 American Institute of Aeronautics and Astronautics Inc. (AIAA). https://doi.org/10.2514/6.2018-4228

A Preliminary Sizing Method for Hybrid-Electric Aircraft Including Aero-Propulsive Interaction Effects

Reynard de Vries*, Malcom Brown† and Roelof Vos‡
Delft University of Technology, Delft, 2629HS, The Netherlands

The potential benefits of hybrid-electric propulsion (HEP) have led to an increased interest in this topic over the past decade. One promising advantage of HEP is the distribution of power along the airframe, which enables synergistic configurations with improved aerodynamic and propulsive efficiency. The purpose of this paper is to present a generic sizing method suitable for the first stages of the design process of hybrid-electric aircraft, taking into account the powertrain architecture and associated propulsion–airframe integration effects. To this end, the performance equations are modified to account for aero-propulsive interaction. A power-loading constraint-diagram is used for each component in the powertrain to provide a visual representation of the design space. The results of the power-loading diagrams are used in a HEP-compatible mission analysis and weight estimation to compute the wing area, powerplant size, and take-off weight. The resulting method is applicable to a wide range of electric and hybrid-electric aircraft configurations and can be used to estimate the optimal power-control profiles. For demonstration purposes, the method is applied a HEP concept featuring leading-edge distributed-propulsion (DP). Three powertrain architectures are compared, showing how the aero-propulsive effects are inlcuded in the model. The results confirm the method is sensitive to top-level HEP and DP design parameters, and indicate an increase in wing loading and power loading enabled by DP.

I. Introduction

In order to meet the stringent sustainability goals established by NASA [1] and the European Commission [2], numerous aircraft concepts featuring distributed propulsion have appeared in the last decade [3–11]. Distributed-propulsion systems promise improvements in aero-propulsive efficiency through, for example, reduced wing area [3, 8] or increased effective bypass ratio [4]. This recent growth in distributed-propulsion concepts can be attributed to the development of hybrid-electric powertrains. While *distributed propulsion* (DP) implies spreading the propulsive elements (i.e., fans, propellers, or jets) over the airframe in a beneficial manner [12, 13], *hybrid-electric propulsion* (HEP) refers to the use of two energy types (electrical and chemical) in the generation and transmission of power. Compared to fully electric configurations, HEP allows larger aircraft and increased ranges, due to a lower battery mass [14]. Although HEP can be used with different propulsion-system layouts, it presents a synergistic benefit when combined with distributed propulsion, due to the versatility that electrical systems offer when it comes to distributing power to the different locations on the airframe. This combination is referred to as hybrid-electric distributed propulsion (HEDP).

Despite the large amount of ongoing research related to hybrid-electric propulsion, little information is available regarding the clean-sheet design process of HEDP aircraft. In many cases, design studies analyze the hybrid-electric powertrain in detail starting from a predefined aircraft configuration [14–16], often maintaining the take-off weight constant [17–19]. Other studies have formulated more generalized conceptual sizing methods for HEP aircraft [19–24], but do not integrate the aero-propulsive interaction effects in the process. These effects cannot be neglected for DP configurations, since they have a large impact on wing and powertrain sizing [3, 25] and, hence, on the overall design of the aircraft. Thus, there is a need to establish a systematic sizing method which accounts for the hybrid-electric powertrain as well as for aero-propulsive interaction effects. The goal of this study is therefore to develop a new conceptual design method which sizes the wing and propulsion system for aircraft featuring HEDP systems.

In the conceptual design method presented in this paper, the traditional preliminary sizing methods [26–29] are modified. A flowchart of the proposed methodology is shown in Fig. 1. First, the thrust, lift and drag decompositions of the aircraft are modified to account for the aerodynamic interaction between the airframe and the propulsors. This leads

---

*PhD Candidate, Faculty of Aerospace Engineering, R.deVries@tudelft.nl, AIAA member.

†Graduate Researcher, Faculty of Aerospace Engineering, M.T.H.Brown@tudelft.nl.

‡Assistant Professor, Faculty of Aerospace Engineering, R.Vos@tudelft.nl, Senior Member AIAA.

to a set of modified constraint equations, which are collected in a wing-loading power-loading diagram to provide a visual representation of the design space. Secondly, the powertrain is modeled by a chain of components rather than a single thermal engine, accounting for two energy sources instead of one. The simplified model considers different HEP operating modes and is sensitive to the corresponding power-control parameters. With this, a power-loading diagram is created for each component in the powertrain. Finally, the aircraft mass is sized for the total energy and power requirements of a specified mission.

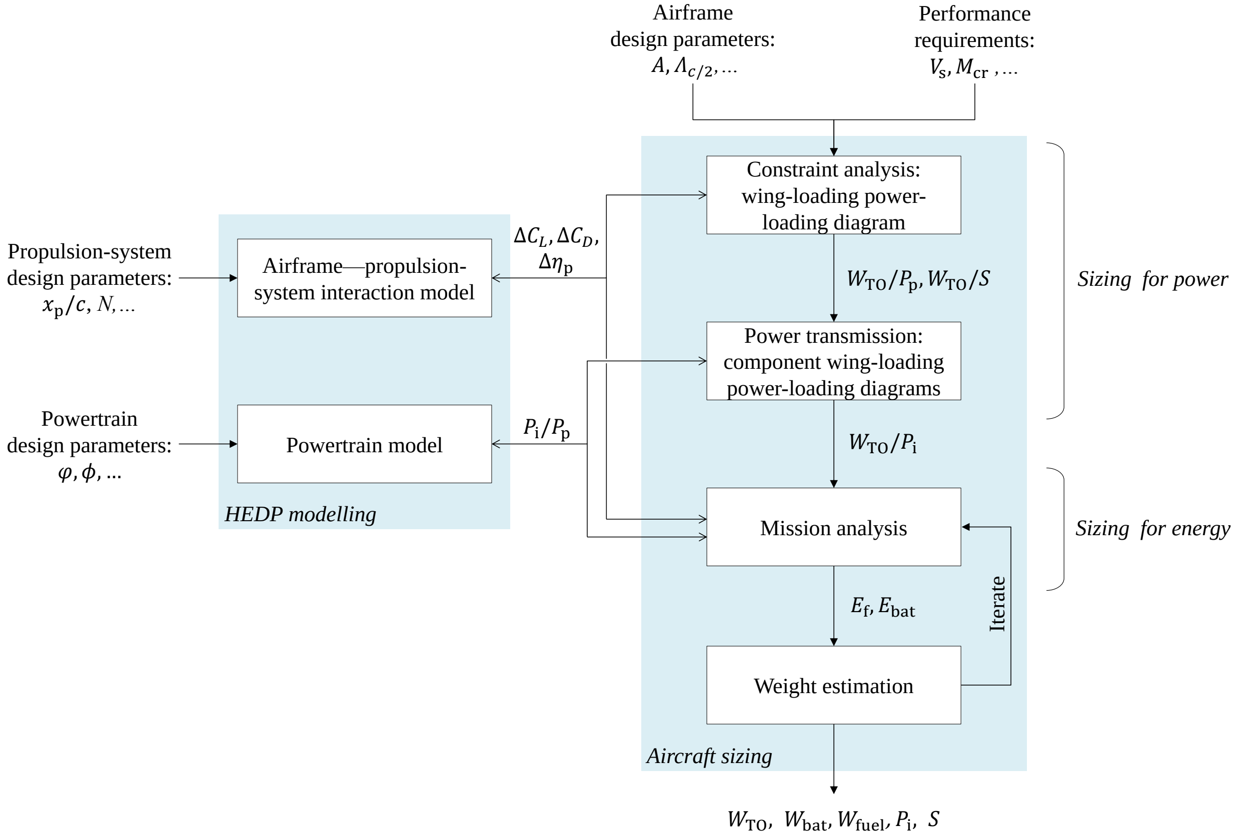

Fig. 1 Simplified flowchart of the proposed design methodology, indicating the sizing modules, HEDP models, and main input/output parameters.

With the proposed method it is possible to rapidly explore the design space, to carry out sensitivity analyses, to estimate the optimal powertrain control parameters, and to evaluate the impact of HEP or DP on the overall performance of the aircraft. Even though the examples described in this paper will focus on wing-mounted DP systems, the rationale followed in this process can easily be extended to other novel propulsor layouts such as tip-mounted propellers or boundary-layer-ingestion systems. Section II describes the aircraft sizing method and powertrain model from a theoretical perspective. Since the airframe–propulsion-system interaction model involves a series of assumptions and semi-empirical methods, it is described separately in a demonstration case specifically focused on aircraft featuring leading-edge DP in Sec. III.

II. Aircraft Sizing Methodology

The purpose of this section is to describe how top-level requirements and design parameters of a HEDP aircraft translate into wing area, installed power, and aircraft weight.

A. Power Constraints: Wing and Powertrain Sizing

The first step in the sizing process is to determine the wing area and installed power of the aircraft. In order to contextualize the problem, two examples of HEDP aircraft layouts are given in Fig. 2. These concepts present multiple sources of thrust, at least one of which—the distributed-propulsion system—has an appreciable effect on the performance of the wing. These characteristics of HEDP configurations must be considered in the lift- and drag decomposition of the aircraft (Sec. II.A.1), which has an impact on the performance equations (Sec. II.A.2) and the resulting constraint diagram (Sec. II.A.3).

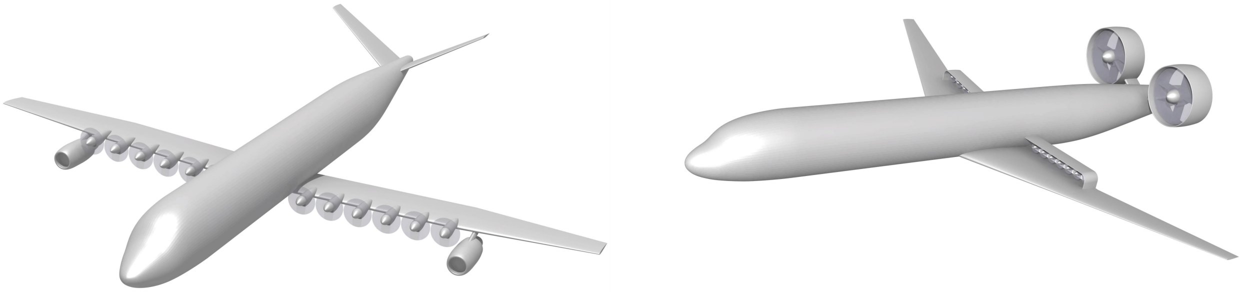

a) Concept 1

b) Concept 2

Fig. 2 Notional representation of two HEDP aircraft: one featuring leading-edge distributed propellers powered by two thermal engines in a serial configuration (a), and one featuring over-the-wing DP combined with a propulsive empennage (b).

1. Thrust, Lift and Drag Decomposition

Due to the aero-propulsive interaction effects that take place between the propulsive elements and the airframe, the aerodynamic performance of the system differs from the combined performance of the two individual components. Conventional sizing methods neglect these effects and therefore thrust and shaft power can be computed independently from lift. This is not the case for advanced propulsion-system layouts such as distributed propulsion. Hence, it is necessary to estimate the forces generated by the system (i.e. lift, drag, and thrust), or, more specifically, to estimate the difference between these forces and the ones that the wing and propulsors[*] would generate separately. For simplicity, the method described here will be limited to aircraft featuring a maximum of two types of propulsors, which entails enough detail to model the concepts depicted in Fig. 2. The rationale followed in the following paragraphs can be extended to a generic number of propulsion systems.

Taking Concept 2 as example, one can distinguish two sources of thrust: the propulsive empennage comprised of two ducted fans at the rear of the fuselage, and the array of distributed propulsors installed over the wing. For demonstration purposes, assume that the propulsive empennage has a negligible effect on the lift and drag of the airframe and vice versa, while the distributed-propulsion array presents strong aerodynamic interaction effects with the wing. In this case, the total thrust of the aircraft T can be expressed as

$$T = T_0 + T_{\text{dp}}, \tag{1}$$

where T_0 is the thrust generated by a propulsive system that has no appreciable impact on airframe performance, and T_{dp} is the thrust generated by a propulsive system which presents strong interaction effects with the airframe. In this example, the thrust produced by the DP system, T_{dp}, will be affected by the presence of the wing. There are several ways to account for the effect of the airframe on propulsor performance. The first is to evaluate the changes in propulsor thrust due to the presence of different elements such as the wing, nacelle, fuselage, and so on [30]. However, since the hybrid-electric powertrain is modeled in terms of power balances (see Sec. II.B), it is preferable to express the interaction effects in terms of changes in propulsive efficiency of the distributed propulsion system (η_{dp}):

$$\eta_{\text{dp}} = \eta_{\text{dp,isolated}} + \Delta\eta_{\text{dp}}(T_{\text{dp}}, L_{\text{airframe}}, S, \ldots). \tag{2}$$

Here T_{dp} is defined as the total force generated by the blades of the distributed propulsors in the installed configuration, $\eta_{\text{dp,isolated}}$ is the propulsive efficiency that these propulsors would have in absence of any other body (ducts[†], nacelles, wing, fuselage, etc.), and $\Delta\eta_{\text{dp}}$ refers to the change in propulsive efficiency when installed on the aircraft. $\Delta\eta_{\text{dp}}$ may depend on geometrical parameters of the wing such as its reference area S, as well as aerodynamic parameters such as

---

[*] The propulsive devices are generally propellers or fans, and are indistinctly referred to as “propulsors” in this paper.

[†] Depending on the type of propulsor, it may be preferable to consider the propulsive device as a fan plus duct, rather than to consider the duct as a part of the airframe. In that case, the contribution of the duct must be included in T_{dp} and $\eta_{\text{dp,isolated}}$, while the change in system (fan and duct) performance is then accounted for in $\Delta\eta_{\text{dp}}$.

L_{airframe}, which is the lift generated by the aircraft when no thrust is produced. At this stage, the effect of the spinner and the normal (in-plane) forces on the propulsors are neglected, and therefore the thrust vector is aligned with the propulsor axis. For a more accurate computation, the normal propeller forces should be included, especially at high incidence angles [31] (e.g. in the case of thrust vectoring). Moreover, in Eq. 2 the propulsive efficiency is defined as $\eta_{\mathrm{dp}} = T_{\mathrm{dp}} V / P_{\mathrm{s,dp}}$, where V is the freestream velocity magnitude and $P_{\mathrm{s,dp}}$ is the combined shaft power of the distributed propulsion array. However, for configurations with significant inflow distortion—such as boundary-layer ingestion concepts—the previous definition is not valid since it may lead to propulsive efficiencies greater than one [32]. In that case, a different parameter must be used, such as for example the power-saving coefficient [11, 32, 33] or alternative definitions of propulsive efficiency, as proposed by other authors [34, 35].

The airframe lift included in Eq. 2, L_{airframe}, can be related to the total lift generated by the aircraft L through

$$L = L_{\mathrm{airframe}} + \Delta L(T_{\mathrm{dp}}, L_{\mathrm{airframe}}, S, \ldots), \tag{3}$$

where ΔL is the increase in aircraft lift due to the thrust generated be the propulsors. ΔL depends on thrust of the distributed propulsion system and other operational and geometrical parameters of the aircraft, and does not include the effective lift increase due to thrust vectoring. The effect of aero-propulsive interaction on the overall drag of the aircraft is included as follows:

$$D = D_0 + \Delta D_0(T_{\mathrm{dp}}, S, \ldots) + D_{\mathrm{i}}(L_{\mathrm{airframe}}) + \Delta D_{\mathrm{i}}(T_{\mathrm{dp}}, L_{\mathrm{airframe}}, S, \ldots), \tag{4}$$

where D_0 is the zero-lift drag of the aircraft when no DP system is present, and ΔD_0 is the increase in zero-lift drag due to the DP system. This increase can caused by interaction with jets or slipstreams at zero lift, by variations in angle of attack in order to maintain zero lift, or by changes in wetted area due to pylons, nacelles, and other external elements of the propulsion-system installation. The last contribution is, in first approximation, independent of thrust, but has been included in ΔD_0 nonetheless since it depends on the type of propulsion system considered. Additionally, D_{i} is the lift-induced drag of the airframe without propulsion system, and ΔD_{i} is the change in lift-induced drag due to thrust, that is, the difference between the drag of the complete aircraft with the propulsor at a determined thrust setting, and the drag that would exist at $T_{\mathrm{dp}} = 0$ for the same total lift value. Although different drag breakdowns exist [30, 36, 37], this simplified approach has been selected because it clearly identifies the contribution of the installation effects. All lift and drag contributions can be expressed as non-dimensional coefficients by dividing them by the reference area of the wing S and the dynamic pressure of the freestream q_∞. For the lift-induced drag coefficient of the airframe, a parabolic lift polar is assumed (i.e., $C_{D_i} = C^2_{L_{\mathrm{airframe}}}/(\pi A e)$, where A is the aspect ratio of the wing and e the Oswald factor).

In order to incorporate the aero-propulsive interaction effects in the sizing process, these "Delta" terms (lift, drag, and propulsive efficiency) have to be estimated. Since an accurate estimation of the Delta components requires detailed aerodynamic analyses, they are often only included in the later stages of the design loop. For the conceptual sizing phase, surrogate models or simplified aerodynamic models are required to estimate this effect. An example of how this can be done for leading-edge-mounted propellers is provided in Sec. III.

2. *Derivation of Performance Constraint Equations*

The main forces acting on the aircraft are represented in Fig. 3. While traditional sizing methods consider a single thrust vector which forms a small angle with respect to the velocity vector of the aircraft [27], for HEDP aircraft, multiple thrust sources must be considered, as discussed previously. Here it is assumed that T_0 is aligned with the velocity vector for simplicity, while the thrust vector of the DP system can be deflected an angle α_{p} if, for example, the propulsors are installed on a flap, or if the jet or slipstream is deflected [6].

In Fig. 3, W is the weight of the aircraft, V its velocity vector, γ the flight path angle, and μ the bank angle. By applying Newton's second law along the X', Z' and Y axes respectively, one obtains the following equilibrium equations:

$$T_0 + T_{\mathrm{dp}} \cos\alpha_{\mathrm{p}} - W \sin\gamma - D = \frac{W}{g}\frac{\mathrm{d}V_{X'}}{\mathrm{d}t}, \tag{5a}$$

$$L \cos\mu + T_{\mathrm{dp}} \sin\alpha_{\mathrm{p}} \cos\mu - W \cos\gamma = \frac{W}{g}\frac{\mathrm{d}V_{Z'}}{\mathrm{d}t}, \tag{5b}$$

$$L \sin\mu + T_{\mathrm{dp}} \sin\alpha_{\mathrm{p}} \sin\mu = \frac{W}{g}\frac{\mathrm{d}V_{Y}}{\mathrm{d}t}. \tag{5c}$$

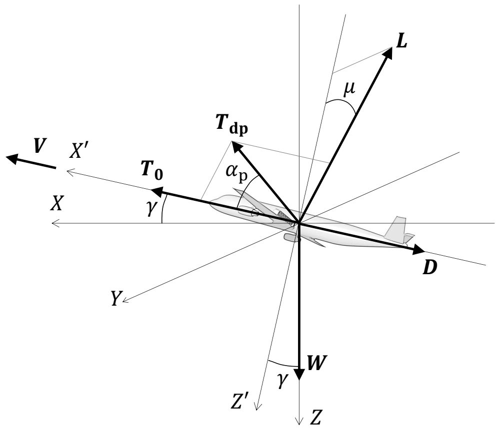

Fig. 3 Schematic representation of the forces acting on the aircraft point model. The X' and Z' axes result from an aircraft rotation of magnitude γ of the X and Z axes around the Y axis. The vector $\boldsymbol{L}$ is contained in the plane defined by the Y and Z' axes, while the vector $\boldsymbol{T}_{\mathrm{dp}}$ is contained in the plane defined by the vectors $\boldsymbol{L}$ and $\boldsymbol{D}$.

In Eqs. 5a, 5b and 5c, g is the gravitational acceleration, and $\mathrm{d}V_{X'}/\mathrm{d}t$, $\mathrm{d}V_Y/\mathrm{d}t$ and $\mathrm{d}V_{Z'}/\mathrm{d}t$ are the acceleration of the aircraft along the X', Y and Z' axes respectively. The acceleration along the Z' axis is assumed to be zero for all maneuvers considered here. $\mathrm{d}V_Y/\mathrm{d}t$ represents the centrifugal acceleration, which can be computed as:

$$\frac{\mathrm{d}V_Y}{\mathrm{d}t} = \frac{V^2}{R_{\mathrm{turn}}}, \tag{6}$$

where R_{turn} is the local turn radius of the aircraft trajectory. The flight path angle of the aircraft γ can be related to the climb rate $c = \mathrm{d}h/\mathrm{d}t$ (where h is altitude of the aircraft) through:

$$\sin\gamma = \frac{c}{V}. \tag{7}$$

Defining the ratio between the thrust of the DP array and the total thrust of the aircraft as $\chi = T_{\mathrm{dp}}/T$, the force equilibrium along the X' axis (Eq. 5a) can be expressed as:

$$\frac{T}{W} = \frac{1}{1-\chi(1-\cos\alpha_{\mathrm{p}})}\left(\frac{D}{W} + \frac{c}{V} + \frac{1}{g}\frac{\mathrm{d}V}{\mathrm{d}t}\right), \tag{8}$$

where the term on left hand side of the equation is the total thrust-to-weight ratio of the aircraft. Applying the drag breakdown given by Eq. 4 and expressing the contributions as non-dimensional coefficients leads to:

$$\frac{T}{W} = \frac{\dfrac{q_\infty}{(W/S)}\left[C_{D_0} + \Delta C_{D_0}\left(\chi\dfrac{T}{W}, \dfrac{W}{S}, \ldots\right) + \dfrac{C^2_{L_{\mathrm{airframe}}}}{\pi A e} + \Delta C_{D_{\mathrm{i}}}\left(\chi\dfrac{T}{W}, C_{L_{\mathrm{airframe}}}, \dfrac{W}{S}, \ldots\right)\right] + \dfrac{c}{V} + \dfrac{1}{g}\dfrac{\mathrm{d}V}{\mathrm{d}t}}{1-\chi(1-\cos\alpha_{\mathrm{p}})}. \tag{9}$$

Given that the aircraft size is unknown at this stage, it is important to express the “Delta” terms as a function of normalized variables such as thrust-to-weight ratio or wing loading. For conventional aircraft, the ΔC_{D_0} and $\Delta C_{D_{\mathrm{i}}}$ terms in Eq. 9 are zero and the airframe lift coefficient can be related to wing loading through $C_{L_{\mathrm{airframe}}} = (W/S)/q_\infty$, and therefore T/W can explicitly be computed as a function of wing loading for a given flight condition. However, in DP configurations the airframe lift coefficient is not known a priori. Therefore, Eq. 9 is coupled to the equilibrium of forces along the Z' axis, and can no longer be evaluated independently. By inserting the lift decomposition provided by Eq. 3 in Eq. 5c and reorganizing terms, the equilibrium of forces in Z' direction can be expressed as:

$$\frac{W}{S} = \frac{q_\infty \cos\mu\left[C_{L_{\mathrm{airframe}}} + \Delta C_L\left(\chi\dfrac{T}{W}, C_{L_{\mathrm{airframe}}}, \dfrac{W}{S}, \ldots\right)\right]}{\sqrt{1-\left(\dfrac{c}{V}\right)^2} - \chi\sin\alpha_{\mathrm{p}}\cos\mu\left(\dfrac{T}{W}\right)}. \tag{10}$$

Equations 9 and 10 can be solved to obtain a combination of T/W and W/S which guarantees equilibrium flight for a given velocity and airframe lift coefficient. If $\Delta C_L, \Delta C_{D_0}, \Delta C_{D_\mathrm{i}} = f\left(\chi(T/W), C_{L_\mathrm{airframe}}, (W/S), ...\right)$ are simple functions, Eqs. 9 and 10 can be combined to form a single analytical solution. However, since the "Delta" functions can be arbitrarily complicated, in most cases Eqs. 9 and 10 have to be solved iteratively.

Performance requirements for turn maneuvers can be expressed in terms of bank angle, turn radius, turn rate, or load factor. If the required bank angle is specified, Eqs. 9 and 10 can be solved as explained in the previous paragraphs. However, if the turn radius R_turn is given as a requirement instead, the bank angle has to be computed from the equilibrium of forces along the Y axis. This is possible by reorganizing and substituting the terms in Eq. 5b:

$$\sin\mu = \frac{\dfrac{1}{g}\dfrac{V^2}{R_\mathrm{turn}}}{\dfrac{q_\infty}{W/S}\left[C_{L_\mathrm{airframe}} + \Delta C_L\left(\chi\dfrac{T}{W}, C_{L_\mathrm{airframe}}, \dfrac{W}{S}, ...\right)\right] + \chi\sin\alpha_\mathrm{p}\left(\dfrac{T}{W}\right)}. \tag{11}$$

On the other hand, if the turn rate ω is specified, this can be related to the turn radius through $V = \omega R_\mathrm{turn}$. Finally, if the load factor $n = L/W$ is specified as requirement, this parameter can be related to the bank angle by dividing Eq. 5c by W and regrouping the terms to obtain

$$\cos\mu = \frac{\sqrt{1-\left(\dfrac{c}{V}\right)^2}}{n + \chi\sin\alpha_\mathrm{p}\left(\dfrac{T}{W}\right)}. \tag{12}$$

3. Constructing the Performance Constraints Diagram

The performance constraint diagram is a well-established method [26–28] used to represent the different performance constraints of the aircraft and the resulting feasible design space in terms of wing loading and power loading or thrust-to-weight ratio. In most cases, thrust-to-weight ratio (T/W) is used on the y-axis of the diagram for turbofan aircraft, while power loading (W/P) is used for propeller aircraft. However, for HEDP aircraft, a power-loading diagram is preferred independently of the type of propulsor for several reasons. Firstly, the power produced by the propulsive elements is required to size the components of the powertrain, and not thrust (see Sec. II.B). Secondly, when selecting the optimum design, it makes more sense to select the powertrain that has to produce least power (since this is directly tied to the energy consumption), and not the one that has to produce least thrust. In the following paragraphs, the equations of motion derived in the previous section will be presented in a thrust-to-weight-ratio diagram and subsequently translated into a power-loading diagram.

For a given flight condition and airframe lift coefficient, Eqs. 9 and 10 generate the two curves shown Fig. 4. The intersection of these curves gives the equilibrium flight point $[(W/S)_\mathrm{eq},(T/W)_\mathrm{eq}]$, that is, the combination of T/W and W/S where the required flight condition is satisfied without any additional accelerations. Along the "Z'-equilibrium" curve, the aircraft presents no acceleration in Z' direction, and its specific excess power can be either positive or negative. The specific excess power (SEP) can be obtained through manipulation of Eq. 8, rearranging the terms such that:

$$\mathrm{SEP} = \frac{\mathrm{d}}{\mathrm{d}t}\left(h + \frac{V^2}{2g}\right) = \frac{\left(1-\chi\left(1-\cos\alpha_\mathrm{p}\right)\right)T - D}{W}V. \tag{13}$$

Equation 13 shows that, along the Z'-equilibrium curve, the aircraft can either climb or accelerate in X' direction if $T/W > (T/W)_\mathrm{eq}$ (i.e., SEP > 0), or descend or decelerate if $T/W < (T/W)_\mathrm{eq}$ (i.e., SEP < 0). Analogously, the "X'-equilibrium" curve represents the loci of points where SEP $= 0$. Along this curve, the aircraft accelerates in the negative Z' direction if $T/W > (T/W)_\mathrm{eq}$, or in positive Z' direction if $T/W < (T/W)_\mathrm{eq}$. Note that, at zero thrust-to-weight ratio, T_DP is zero, and thus the Z'-equilibrium curve attains the wing-loading value that would be obtained if the aero-propulsive interaction effects were neglected: $(W/S)_{T_\mathrm{dp}=0} = q_\infty C_{L_\mathrm{airframe}}$. The potential benefit of distributed propulsion can clearly be identified in Fig. 4: for a given airframe lift coefficient, the wing loading of the aircraft can be increased from $(W/S)_{T_\mathrm{dp}=0}$ to $(W/S)_\mathrm{eq}$, if $\Delta C_L > 0$.

The discussion in the previous paragraph assumes a given flight speed and airframe lift coefficient, and thus the solution of Eqs. 9 and 10 provides a single point in the diagram. In order to obtain performance constraint *curves*, either the velocity or the airframe lift coefficient must be varied parametrically. Taking this into consideration, four types of performance constraints can be distinguished:

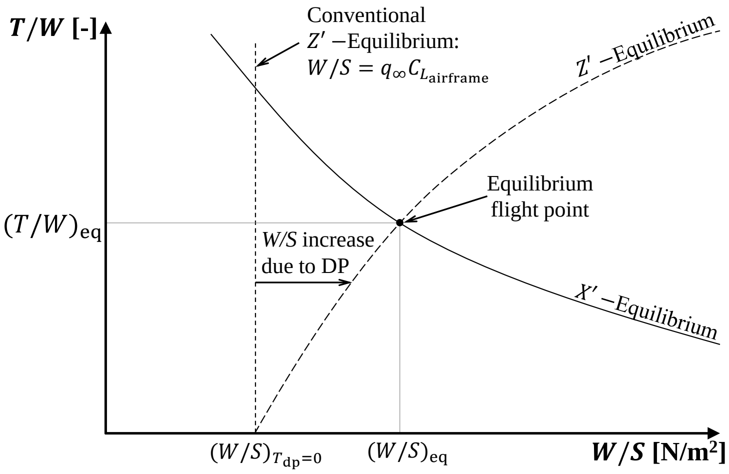

Fig. 4 Notional wing-loading versus thrust-to-weight-ratio diagram indicating the curves obtained from the equilibrium of forces along the X' axis (Eq. 9) and Z' axis (Eq. 10) for a given velocity and airframe lift coefficient.

- Constraints at constant flight speed: this is the case of e.g. the cruise speed constraint. A notional example is represented in Fig. 5a. As the assumed airframe lift coefficient increases while keeping the flight speed constant, a smaller wing (i.e. higher wing loading) is required to generate the same total lift.
- Constraints at constant airframe lift coefficient: this occurs when a stall margin has to be maintained. For example, if a climb gradient requirement must be met at 1.4 times the reference stall speed V_{SR}, then the aircraft must be able to fly at $C_{L_{\max}}/1.4^2$, where $C_{L_{\max}}$ is the total maximum lift coefficient (including aero-propulsive effects[‡]). In this case, the resulting velocity at which the maneuver must be performed increases with increasing wing loading.
- Constraints at fixed flight speed and airframe lift coefficient: in for example a stall speed constraint, the aircraft must be able to achieve a determined speed at $C_{L_{\max}}$. Since both parameters are fixed, a single point in the diagram is obtained. For resemblance with conventional wing-loading diagrams, in this paper a vertical line is drawn at the wing loading corresponding to the point obtained. This line indicates a wing loading that cannot be exceeded under any circumstances; however, it should be noted that this wing-loading value can only be achieved at a single thrust-to-weight ratio or power loading. Since the thrust or power required for this flight condition is, in general, not limiting, the engines must be set to a predetermined thrust setting once the powertrain has been sized by one of the other more limiting constraints. If the pilot were to decrease the thrust setting at maximum wing loading, the aircraft would stall not only due to its deceleration, but also because the change in lift due to thrust (ΔC_L) would decrease. Moreover, it is interesting to add that if C_{D_0} is increased during approach by means of, for example, speed brakes, additional thrust would have to be provided to maintain a constant speed, thus increasing ΔC_L and, subsequently, the maximum wing loading.
- Semi-empirical constraints: during take-off and landing, Eqs. 5a, 5b and 5c are not applicable due to the forces exerted on the runway surface. One could include these forces in the point model, but even in that case, detailed knowledge or an empirical relation of the engine thrust lapse with velocity would be required. Hence, semi-empirical methods [26, 29] are used to determine the take-off distance and landing distance constraints. In this paper, the take-off-parameter (TOP) described by Raymer [29] is used.

The resulting constraint curves, which have been expressed in terms of thrust-to-weight ratio, can be related to a power loading (W/P_{p}) diagram using:

$$\frac{W}{P_{\mathrm{p}}} = \frac{1}{V(T/W)}. \tag{14}$$

[‡] In this paper it is assumed that future airworthiness regulations will change such that the performance requirements can be met in powered conditions, instead of in engine-idle conditions. Although this is change currently subject to debate [36], it should be kept in mind that some of the benefits of distributed-propulsion systems cannot be achieved with the current regulations.

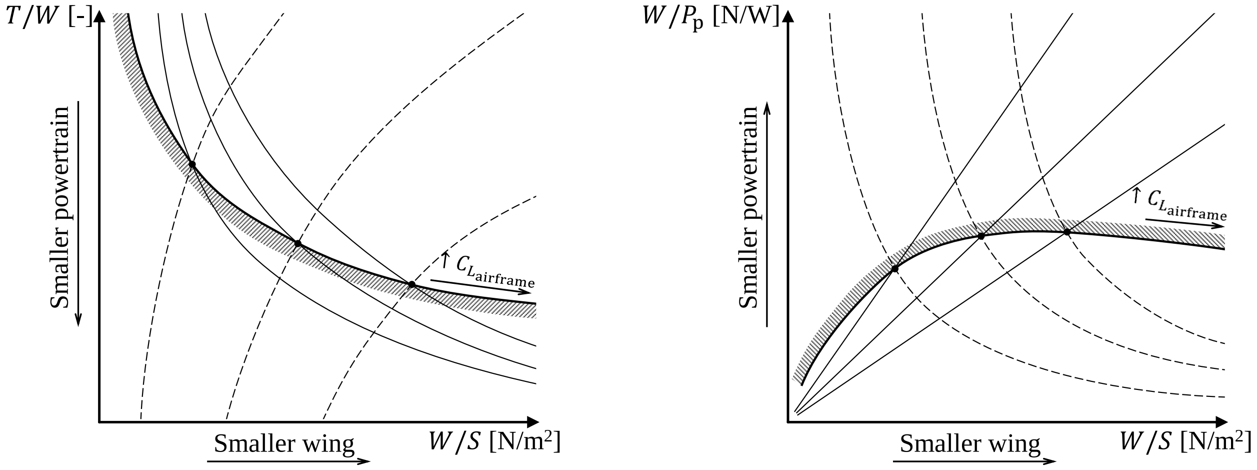

a) Thrust-to-weight ratio

b) Power loading

Fig. 5 Notional wing-loading versus thrust-to-weight-ratio diagram (a) and wing-loading power-loading diagram (b), indicating the constraint curve obtained by evaluating the equilibrium flight points for different airframe lift-coefficient values at constant flight speed.

The power-loading constraint curve obtained is shown in Fig. 5b. Power is used as denominator in the power-loading variable for consistency with established methods [26]. Note that the *propulsive* power ($P_\text{p} = TV$) is used in this first power-loading diagram, rather than the shaft power used in traditional power-loading diagrams. The propulsive power is related to the shaft power by means of the powertrain model described in the following section. Finally, the different constraints can be represented in the same power-loading diagram by correcting each constraint to maximum take-off weight W_TO. This can be done by assuming a weight fraction $f_W = W/W_\text{TO}$ for each flight condition, such that $(W_\text{TO}/P) = (W/P)/f_W$.

B. Hybrid-Electric Powertrain Modeling

Given that a hybrid-electric powertrain is constituted of a chain of components rather than a single gas turbine, a simplified powertrain model is required to link the propulsive power produced by the system to the power required from the different powertrain components and its energy sources. The prerequisites for the model are:

- It must require only a limited amount of input variables, which are known in the preliminary sizing phase.
- It must be sensitive to different powertrain architectures.
- It should be able to account for multiple propulsion systems.
- It must account for component failure.
- It must be compatible with the charging of batteries and energy harvesting[§].
- It should be sensitive to a series of power-control parameters which allow a posterior analysis and optimization of power settings along the mission.

In order to be able to meet all these prerequisites simultaneously, a series of simplifications are required:

- The system is treated as steady-state, i.e. no transient effects are included
- A constant conversion/transmission efficiency is assumed per component
- The effect of battery state-of-charge and system voltage are not considered
- No cooling system is included in the model
- Losses in the cables are not included or, at least, are not dependent on system voltage or cable length

Although these simplifications limit the accuracy and applicability of the model, the approach is considered sensitive enough for the preliminary sizing phase. The following two subsections present the different powertrain architectures

---

[§] While the examples provided in this paper will not consider energy harvesting, this requisite is included for possible future applications. For example, increasing drag during approach by windmilling one set of propulsors while powering the other set to increase wing lift could have a significant impact on wing sizing.

considered and the control parameters used to define their behavior, respectively. Subsection II.B.3 then shows the manner in which the different unknowns can be computed, followed by a discussion in Subsection II.B.4 on how battery charging or energy harvesting should be incorporated. Finally, a discussion is held regarding the application of the model to the sizing process in Subsection II.B.5.

1. Hybrid-Electric Powertrain Architectures

After reviewing different conceptual HEP powertrain sizing methods [19, 20, 22, 38–40] it has become evident that no conceptual model exists which is applicable to any powertrain layout, while being sensitive to the different powertrain architectures. Although there are tools which can calculate the power balance across any given powertrain architecture [19, 38], this requires the designer to manually specify and link each component of the powertrain, thus making it inappropriate for the very first steps of a clean-sheet design process. Therefore, this paper proposes a method based on a set of predefined powertrain architectures. The architecture classification followed in this process was proposed by Felder [41] and later adopted by the National Academy of Sciences [42]. Although this classification cannot represent an arbitrarily-complicated HEP powertrain, it covers the majority—if not all—of the HEP concepts studied until today.

The configurations and nomenclature proposed by Felder, including a conventional powertrain for reference, are shown in the first six architectures of Fig. 6. The simplified representations include energy sources, components which split power, components which transform one type of power into another, and the power paths that connect these elements. Components such as inverters or transformers are not explicitly modeled, since they do not change the type of power transmitted, and their weight and efficiency losses can be included in the associated electrical machines or in the power management and distribution (PMAD, or "PM") component. The components are divided into the elements which constitute the "primary" powertrain, and those that constitute the "secondary" powertrain. The primary components are, directly or indirectly, mechanically coupled to the gas turbine. The secondary components include the devices which power the electrically-driven propulsion system. The primary and secondary branches of the powertrain contain N_1 and N_2 identical instances of each component, respectively. For example, the concept shown in Fig. 2a contains two gas turbines which constitute the primary powertrain branch ($N_1 = 2$), and twelve propulsors driven by electromotors which form part of the secondary powertrain branch ($N_2 = 12$).

Upon closer inspection of the first six powertrain configurations shown in Fig. 6, it becomes evident that the first five are, in essence, limit cases of the sixth (the serial/parallel partial hybrid, SPPH). Thus, the SPPH architecture can be used as a generic model, while the remaining architectures can be obtained by setting specific power-control parameters to zero or one. After a more detailed analysis of the SPPH, three additional limit cases are identified (Configurations 7–9) which are fully electrical powertrains. Since Configurations 7 and 8 are essentially the same, their definition is redundant, although they have been included nonetheless for consistency.

2. Definition of Power Control Parameters

The SPPH architecture contains two nodes: a gearbox and a PMAD system. Therefore, one can already anticipate that two parameters are necessary in order to completely define the behavior of the system, in addition to one extensive parameter which dictates how much power the system must actually produce. In other words, the number of input parameters required to size the components of an arbitrary powertrain architecture equals to the number of nodes plus one. The authors of previous studies [14, 20, 23, 43] have used different parameters to describe the powertrain, and it appears no consensus has been reached with respect to the nomenclature and definition of these variables. Consequently, the parameters proposed here are based on previous definitions, but have been modified such that specific combinations of the power-control parameters can define the powertrain architecture.

The first parameter is the *supplied power ratio*, which can be expressed as

$$\Phi = \frac{P_{\mathrm{bat}}}{P_{\mathrm{bat}} + P_{\mathrm{f}}}. \tag{15}$$

The supplied power ratio represents the amount of power drawn from the electrical energy source (batteries) with respect to the total amount of power drawn from all energy sources (battery plus fuel, in this case) for a given point along the mission. Hence, this parameter is only non-zero for powertrains containing batteries (configurations 3, 4 and 6–9). In normal operation, the battery is discharging and thus $\Phi \in [0, 1]$. However, if the battery is being charged ($P_{\mathrm{bat}} < 0$), this parameter is negative or greater than one. This definition of supplied power ratio differs from the original one by Isikveren et al. [20] and the alternative definition by Voskuijl et al. [14] in the sense that it is a time-dependent control parameter, and not a scalar property of the aircraft.

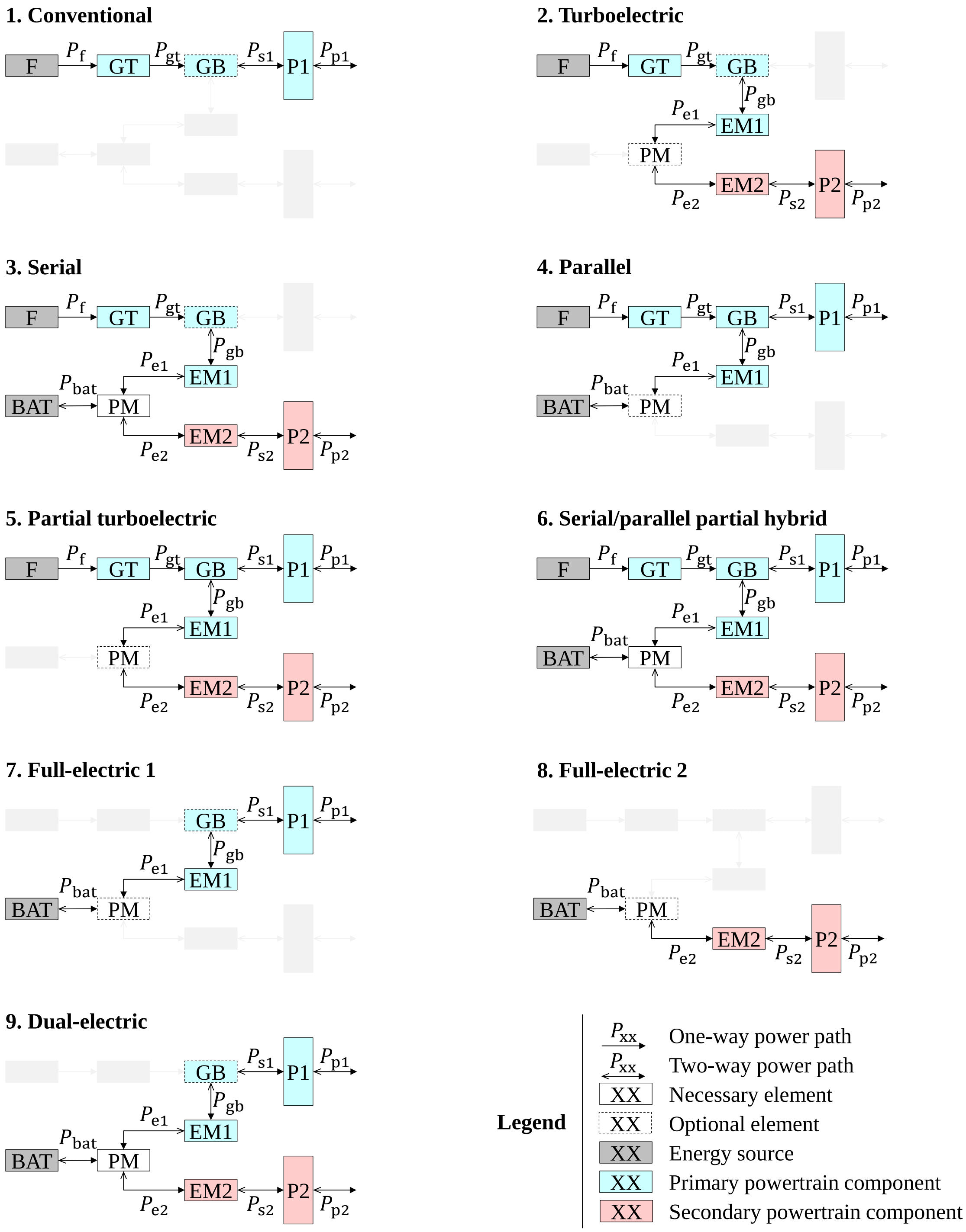

Fig. 6 Simplified models of the different powertrain architectures considered, including the power paths (indicated with lower-case subscripts), and powertrain components and energy sources (indicated with upper-case letters). Lines with two arrow heads indicate paths where the power can flow in both directions, with the positive direction shown by the filled arrowhead. Legend: "F" = fuel, "GT" = gas turbine, "GB" = gearbox, "P" = propulsor, "BAT" = batteries, "EM" = electrical machine (i.e. electromotor or generator), "PM" = power management and distribution system.

The second power-control parameter is the *shaft power ratio*, which represents the amount of shaft power produced by the secondary electrical machines with respect to the total amount of shaft power produced in a given flight condition, that is,

$$\varphi = \frac{P_{\mathrm{s2}}}{P_{\mathrm{s2}} + P_{\mathrm{s1}}}. \tag{16}$$

Analogously to the supplied power ratio, the shaft power ratio belongs to the interval $\varphi \in [0, 1]$ during normal operation (when both propulsion systems are generating thrust), but is negative or greater than 1 if one or both of the propulsion systems are windmilling (i.e., extracting energy from the flow). The relations between the two power-control parameters and the nine powertrain layouts considered are collected in Table 1.

Table 1 Characteristics of the nine powertrain architectures considered, indicating the values of supplied power ratio and shaft power ratio associated to each one, as well as the remaining number of degrees of freedom (DOF) which must be fixed in order to solve the system. A dot (·) indicates any value can be used.

Configuration	Φ	φ	N° DOF
1. Conventional	0	0	1
2. Turboelectric	0	1	1
3. Serial	·	1	2
4. Parallel	·	0	2
5. Partial TE	0	·	2
6. S/P partial hybrid	·	·	3
7. Full-electric 1	1	0	1
8. Full-electric 2	1	1	1
9. Dual-electric	1	·	2

Apart from these two power control parameters, the conventional gas turbine throttle parameter is defined as

$$\xi_{\mathrm{GT}} = \frac{P_{\mathrm{GT}}}{P_{\mathrm{GT,max}}}, \tag{17}$$

which represents the power produced by the gas turbine with respect to the maximum power it can produce in the given flight condition. This power can in turn be related to the installed sea-level static power of the gas turbine $P_{\mathrm{GT,max,SLS}}$ by means of an altitude and velocity lapse. In this paper, the altitude lapse provided by Ruijgrok [44] is applied, and the velocity lapse is neglected. For the fully-electric architectures (Configurations 7–9), where no gas turbine is used, an analogous "electrical machine throttle" is used instead:

$$\xi_{\mathrm{EM}} = \frac{P_{\mathrm{EM}}}{P_{\mathrm{EM,max}}}. \tag{18}$$

In Eqs. 17 and 18 the subscripts contain upper-case letters. These refer to a *component* of the powertrain, while lower-case letters refer to a *power path* (indicated by arrows in Fig. 6). Although the "installed" gas turbine power evidently refers to the shaft power it can produce (i.e. $P_{\mathrm{GT}} = P_{\mathrm{gt}}$), for an electrical machine this distinction is necessary. For example, the "installed" electrical machine power P_{EM2} could either be equal to P_{e2} or P_{s2}, depending on whether it is acting as an electromotor or as a generator, as discussed in Subsection II.B.5.

Finally, it is necessary to link the power-control parameters to the performance constraint equations derived in Sec. II.A.2. In this process, two thrust sources were assumed, T_0 and T_{dp}. Logically, the use of two thrust sources is only compatible with powertrain architectures that present two types of propulsion system (i.e., configurations 5, 6, and 9). For the other architectures, either T_0 or T_{dp} has to be zero. If the aircraft does present two propulsion systems, then the thrust ratio χ can be related to the shaft power ratio φ through

$$\chi = \begin{cases} \dfrac{1}{1 + \dfrac{\eta_{\mathrm{p2}}}{\eta_{\mathrm{p1}}}\left(\dfrac{\varphi}{1-\varphi}\right)}, & \text{if the DP system belongs to the primary powertrain branch,} \\[4ex] \dfrac{1}{1 + \dfrac{\eta_{\mathrm{p1}}}{\eta_{\mathrm{p2}}}\left(\dfrac{1-\varphi}{\varphi}\right)}, & \text{if the DP system belongs to the secondary powertrain branch,} \end{cases} \tag{19}$$

where η_{p1} and η_{p2} are the propulsive efficiencies of the propulsors of the primary and secondary powertrain branches, respectively. The propulsive efficiency given by Eq. 2 corresponds to either η_{p1} or η_{p2}, depending on whether the DP system is installed on the primary or secondary powertrain branch. With Eq. 19 it is evident that χ and φ represent the same degree-of-freedom, but χ refers to the *propulsive* power share of the DP system (which can correspond to either the primary or secondary powertrain branch), while φ refers to the *shaft* power share of the secondary, electrically-driven, propulsor system. Furthermore, if φ is not in the interval [0,1] because one or both of the propulsion systems are harvesting energy, then χ is also negative or greater than one. Thus, the thrust-to-weigh ratio obtained from the performance equations will change accordingly. In these circumstances, a "windmilling efficiency" must be assumed for the propulsors, since it may differ appreciably from their propulsive efficiency.

3. Solving the Powertrain Equations

The powertrain model has ten unknowns, corresponding to the ten power paths shown in Fig. 6.6. Thus, ten equations are necessary to solve the system. The first seven can be obtained by applying a power balance across each component. For a generic component i, this equation is expressed as:

$$\sum P_{\mathrm{out}} = \eta_i \sum P_{\mathrm{in}}, \tag{20}$$

where the left-hand side indicates the summation of power paths flowing "out" of the component, and the right-hand side represents the summation of power paths flowing "in" to the component, multiplied by the conversion efficiency of the component, η_i.

Three additional equations or values are required. This ties in to the discussion of Sec. II.B.2, which stated that three parameters have to be specified in order to define the complete behavior of the powertrain. For example, Φ (which relates P_{bat} to P_{f}), φ (which relates P_{s1} to P_{s2}), and the total required propulsive power $P_{\mathrm{p}} = P_{\mathrm{p1}} + P_{\mathrm{p2}}$ can be specified. The set of linear equations can then be expressed as

$$\begin{bmatrix} -\eta_{\mathrm{GT}} & 1 & 0 & 0 & 0 & 0 & 0 & 0 & 0 & 0 \\ 0 & -\eta_{\mathrm{GB}} & 1 & 1 & 0 & 0 & 0 & 0 & 0 & 0 \\ 0 & 0 & 0 & -\eta_{\mathrm{P1}} & 0 & 0 & 0 & 0 & 1 & 0 \\ 0 & 0 & -\eta_{\mathrm{EM1}} & 0 & 1 & 0 & 0 & 0 & 0 & 0 \\ 0 & 0 & 0 & 0 & -\eta_{\mathrm{PM}} & -\eta_{\mathrm{PM}} & 1 & 0 & 0 & 0 \\ 0 & 0 & 0 & 0 & 0 & 0 & -\eta_{\mathrm{EM2}} & 1 & 0 & 0 \\ 0 & 0 & 0 & 0 & 0 & 0 & 0 & -\eta_{\mathrm{P2}} & 0 & 1 \\ \Phi & 0 & 0 & 0 & 0 & (1-\Phi) & 0 & 0 & 0 & 0 \\ 0 & 0 & 0 & \varphi & 0 & 0 & 0 & (1-\varphi) & 0 & 0 \\ 0 & 0 & 0 & 0 & 0 & 0 & 0 & 0 & 1 & 1 \end{bmatrix} \cdot \begin{bmatrix} P_{\mathrm{f}} \\ P_{\mathrm{gt}} \\ P_{\mathrm{gb}} \\ P_{\mathrm{s1}} \\ P_{\mathrm{e1}} \\ P_{\mathrm{bat}} \\ P_{\mathrm{e2}} \\ P_{\mathrm{s2}} \\ P_{\mathrm{p1}} \\ P_{\mathrm{p2}} \end{bmatrix} = \begin{bmatrix} 0 \\ 0 \\ 0 \\ 0 \\ 0 \\ 0 \\ 0 \\ 0 \\ 0 \\ P_{\mathrm{p}} \end{bmatrix} \tag{21}$$

In Eq. 21, the first seven rows of the coefficient matrix correspond to the power balance equations across the gas turbine, gearbox, primary propulsor, primary electrical machine, PMAD, secondary electrical machine, and secondary propulsor, respectively. The last three rows correspond to the additional information provided, in this case the supplied power ratio, shaft power ratio, and total propulsive power. These three rows can be replaced by different equations, depending on what the designer wants to specify as input to the problem. For example, one could chose to specify the gas turbine throttle ξ_{GT}, P_{p1} and P_{p2} instead. However, if a configuration different than the SPPH is selected, then one or two of these equations will be fixed by Φ and/or φ (see Table 1). For example, if a turboelectric configuration is selected, then $\Phi = 0$ and $\varphi = 1$. In this case, rows 8 and 9 of Eq. 21 are readily determined, and the remaining degree of freedom must be specified in the last row.

The system can be solved by directly inverting the coefficient matrix, since it is relatively small. If this same model is to be used in later design stages when, for example, the dependency of component efficiency on power is accounted for, then an iterative approach will be required. However, at this stage an iterative approach is not recommended, since the solution presents discontinuities, as discussed in the following subsection.

4. In-flight Charging and Energy Harvesting

The signs of the coefficients in Eq. 21 assume that the powers flow as indicated by the filled arrowheads in Fig. 6.6. In this case, the battery is discharging, and both propulsion systems are generating thrust. However, it may also be the case that, for example, during descent the secondary propulsors are windmilling to reduce the approach speed while extracting energy from the flow to recharge the batteries. Although the practical viability or advantages of such technology is subject to investigation, the model includes this possibility for completeness. Under these conditions, the criteria of which power paths flow "in" and "out" of each component in Eq. 20 change, and therefore the efficiency factor multiplies a different term or changes sign in the matrix. This implies that the values in the coefficient matrix are not actually constants, but depend on the direction of the power flows, that is, on the sign of the solution variables. Thus, in a strict sense, the system is not linear.

One possibility would be to assume a given direction of power flows, and to solve the system iteratively, updating the constants in the coefficient matrix based on the sign of the solution of the previous iteration. However, this is not recommended since discontinuities now exist in the solution. The discontinuities exist both in gradient and in value. An example of the former is when the efficiency factor swaps "sides" in the equation because the power flow changes direction. An example of the latter occurs when the battery is charged at a rate exactly equal to the rate at which fuel power is consumed, in which case Φ tends to infinity (see Eq. 15).

A more effective approach, though less elegant, is to assume a given direction of power flow, to construct and solve the corresponding matrix, and to verify the assumption thereafter. If the signs of the powers obtained are different from those assumed, then a different direction of power flow must be considered. Closer inspection of the SPPH architecture reveals that in total nine possible operating conditions exist. This conclusion can be drawn by considering that the gas turbine can only produce positive power, and that not all power paths connected to a given component can simultaneously flow in or out of that component. The nine cases are collected in Table 2, with Eq. 21 corresponding to the first case.

Table 2 Possible operating conditions of the SPPH architecture, defined according to the operation mode of the primary (P1) and secondary (P2) propulsors, batteries (BAT), and primary electrical machines (EM1).

	1	**2**	**3**	**4**	**5**	**6**	**7**	**8**	**9**
P1	thrust	thrust	thrust	thrust	thrust	thrust	harvest	harvest	harvest
P2	thrust	thrust	harvest	thrust	harvest	harvest	thrust	thrust	harvest
BAT	discharge	charge	charge	discharge	discharge	charge	discharge	charge	charge
EM1	generator	generator	generator	motor	motor	motor	generator	generator	generator

Therefore, for the SPPH architecture a total of nine matrices have to be inverted and verified. If a different powertrain architecture is specified, then a number of these combinations are either redundant or not applicable. For example, for a conventional powertrain only case (1) has to be evaluated, while for a serial powertrain the solution can be obtained by solving cases (1), (2) and (3). Finally, although in a most generic sense all the different solutions have to be probed, in most practical applications the designer decides beforehand in which conditions the powertrain is operating for the different points along the mission.

5. Component Sizing

The method described in the previous subsections can be applied to analyze the behavior of the powertrain at any point along the mission. In the sizing process of the powertrain, on the other hand, the maximum installed power is unknown, and must be determined based on all the constraints in the wing-loading–power-loading diagram. Therefore, the propulsive power will always fix one of the three degrees of freedom, while the engine throttle will only be used a posteriori if the constraint must be met at a certain throttle setting.

Since the results from the wing-loading–power-loading diagram are expressed in N/W, the inverse of power loading, $1/(W/P_{\mathrm{p}})$, should be used in the powertrain model, i.e. the powers are computed per unit weight of the aircraft. Once the values of all power paths have been calculated by solving Eq. 21, the limiting values which size each component must be selected. For a generic component, the summation of powers that flow into the component constitute the maximum power that the component has to process (since the output powers are always lower), and thus this value is assumed to be the sizing power. An exception to this rule is the gas turbine, through which the power can only flow in one direction, and the output shaft power is normally used as reference.

Some constraints must be met in "one-engine-inoperative" (OEI) conditions. OEI is interpreted here as the failure of any one component of the powertrain. For the seven powertrain components, the effect of a single component failure can be accounted for by over-sizing all components of the branch where the failure occurs by a factor $N_1/(N_1-1)$ or $N_2/(N_2-1)$, depending on whether the failure occurs in the primary or secondary powertrain branch, respectively. This implies that a single propulsive-power constraint leads to two constraints in the component-power-loading diagrams in OEI conditions, depending on the powertrain branch in which the failure occurs. It is assumed that the failure of a component of the primary powertrain branch does not affect the secondary powertrain branch and vice versa, since they are connected by means of a PMAD system with redundant wiring. Furthermore, the effect of battery pack failure on the powertrain sizing process is not considered.

It is worth adding a final note regarding the selection of the design point. While in conventional power-loading diagrams only one design point exists for minimum installed power, for a hybrid-electric powertrain the wing-loading value corresponding to minimum installed power varies per component. For example, it could occur that the minimum electromotor size is obtained at a different wing loading than the minimum gas turbine size because the two components are limited by different constraints. The design point must therefore be chosen taking into account the power-loading diagrams of all components, and not just based on the propulsive-power loading. Furthermore, since the relative positions of the constraints in the diagram vary per component and depend on the power-control parameters selected, it is important to optimize the power-control laws along the mission, as suggested by previous studies [23].

C. Energy Constraints: Fuel and Battery Sizing

This step of the sizing process calculates the fuel and battery energy required for a determined mission profile and maximum take-off weight (MTOW). Since, at this stage, the power-loading of each component has been determined, the installed power can readily be obtained with an assumed MTOW value. Based on the energy requirements obtained for the mission, the MTOW value must be updated as discussed in Sec. II.D, and the process is repeated iteratively.

The quantity of fuel required to perform the design mission is commonly determined using the Breguet range formula [26–28]. This approach is unsuitable for hybrid electric aircraft since energy consumption does not always relate to a change in aircraft weight, and because the Breguet range equation does not account for aero-propulsive effects. Analytical range formulae have been derived for hybrid-electric aircraft [14, 39, 40], but they depend on the manner in which fuel and electrical energy are used along the mission. A common assumption is that fuel is used during the first part of cruise in order to lighten the aircraft, or that the supplied power ratio remains constant during the mission. This approach does not necessarily result in the optimum overall energy use. Since the power control parameters have a strong impact on block energy consumption [20], the energy sizing method must be applicable for generic power-control profiles. Therefore, no single analytical expression can be used, and a mission analysis is required.

For this reason, a numerical quasi-steady point-model is used, which analyses the instantaneous point performance of the aircraft at suitably small time intervals along the mission. The mission for which the aircraft should be sized varies from case to case, depending on the top-level requirements. For each time step Δt, performance is assumed constant and thus the battery energy (ΔE_{bat}) and fuel energy (ΔE_{f}) consumed in the interval can be estimated as

$$\Delta E_{\mathrm{bat}} = P_{\mathrm{bat}} \Delta t, \tag{22}$$

$$\Delta E_{\mathrm{f}} = P_{\mathrm{f}} \Delta t, \tag{23}$$

where P_{bat} and P_{f} are related to the total propulsive power through the powertrain model described in Sec. II.B. The total propulsive power can be calculated as a function of the flight condition using Eqs. 9, 10 and 14. In this way, the aero-propulsive interaction effects are taken into account. The total energy consumption is then computed by integrating ΔE_{bat} and ΔE_{f} along the entire mission. Note that, while the remaining fuel energy at the end of the mission is generally zero, for the battery energy a minimum state-of-charge (SOC) must be maintained. Furthermore, the battery energy does not necessarily decrease monotonically over time, since the batteries can be recharged during intervals along the mission.

For each mission segment, one can either specify the required propulsive power and leave one power-control parameter undetermined, or provide a profile for each power-control parameter. The first case is characteristic of the cruise phase, where level flight at constant velocity is considered, and hence the propulsive power required is known. In the second case, on the other hand, the resulting SEP is generally non-zero, and thus the aircraft will climb, descend, accelerate, or decelerate. In that case, the ratio between the amount of SEP used for increasing the altitude of the aircraft and the amount used to increase its velocity must also be specified.

D. Weight Estimation

Conventional preliminary sizing methods decompose the take-off weight of the aircraft into payload (W_{PL}), fuel weight (W_{f}) and operating empty weight (W_{OE}, or OEW). Generally, the payload is specified as top-level requirement, while the operating empty weight is estimated as a fraction of MTOW using empirical correlations [26]. For HEP aircraft, the fuel weight can directly be obtained from the fuel energy computed in the mission analysis. However, the OEW can no longer be estimated using empirical correlations, since there is no weight database for HEP aircraft. The weight breakdown of these aircraft differs appreciably from conventional aircraft for several reasons. First of all, the battery weight has to be included in the total aircraft weight. Secondly, the weight of the powertrain is considerably higher for hybrid-electric propulsion systems (see for example Refs. [6–8, 19, 21, 45, 46]). Furthermore, in some cases the wing loading can be significantly higher for HEP concepts [3], and therefore the wing weight fraction will not be comparable to conventional aircraft. Since the weights of these components have a strong impact on the resulting MTOW, it is not possible to carry out a simple “Class-I” weight estimation without taking into account their individual contributions.

The proposed weight breakdown for HEP aircraft is shown in Fig. 7. With this division, the MTOW of the aircraft can be expressed as:

$$W_{\text{TO}} = W_{\text{OE}} + W_{\text{PL}} + W_{\text{f}} + W_{\text{bat}}. \tag{24}$$

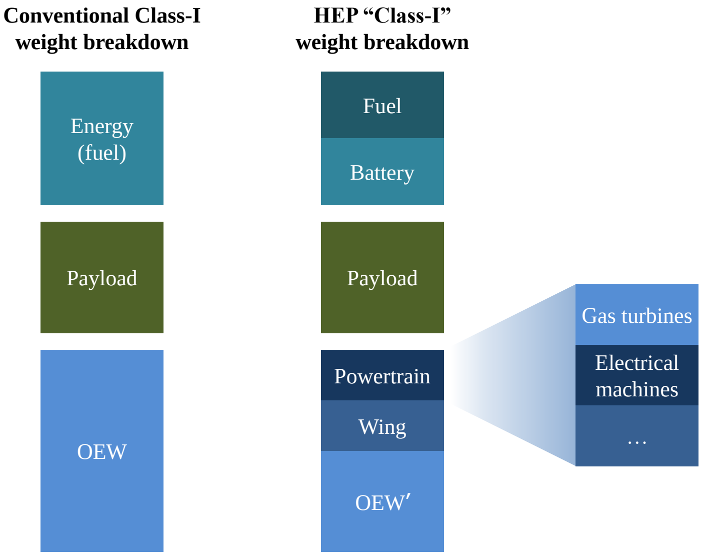

Fig. 7 Comparison between a conventional Class-I aircraft weight breakdown and the modified breakdown applied to HEP configurations.

The weight of the batteries, W_{bat}, can be determined by either energy or power requirements. Both should be evaluated in the sizing process, so as to assure both requirements are met. In terms of energy requirements, the total battery energy consumed during the nominal mission can be divided by the specific energy of the batteries at pack level, e_{bat}, in order to obtain the battery mass. To this amount, a minimum SOC margin (typically around 20% [45, 47]) should be added to avoid reducing the battery cycle life. During the diversion part of the mission, one could decide to reduce this safety margin, since it is an off-design operating point which rarely occurs. In that case, the battery mass requirement is evaluated for both the nominal and the total (nominal plus reserve) mission, each with their respective minimum SOC margin, and the most restrictive case is selected. The maximum power requirement, on the other hand, can be obtained from the design power-loading value obtained in the battery-power-loading diagram, together with an initial guess of the

MTOW, i.e. $P_{\text{bat}} = W_{\text{TO}}/(W_{\text{TO}}/P_{\text{bat}})$. This can, in turn, be converted into a minimum battery mass requirement using the battery's specific power. However, for this the battery's specific power must be estimated at pack level, which not only depends on the battery technology, but also on the way in which the cells are arranged in the aircraft—which is generally unknown at this stage of the design process.

The OEW term of Eq. 24 should be further decomposed in order to distinguish the contribution of the powertrain W_{pt}, as evidenced in earlier studies [22, 24, 45]. Furthermore, for DP concepts, the contribution of the wing W_{w} should be isolated:

$$W_{\text{OE}} = W'_{\text{OE}} + W_{\text{w}} + W_{\text{pt}}. \tag{25}$$

This division is reflected in Fig. 7. In Eq. 25, W'_{OE} is the operating empty weight excluding the powertrain and wing. This component can be estimated by calculating the OEW of a conventional reference aircraft using empirical correlations, and subtracting the weight that the wing and powerplant (i.e., a conventional turboprop, reciprocating engine, or turbofan) would have on that aircraft:

$$W'_{\text{OE}} = W_{\text{OE,ref}} - W_{\text{w,ref}} - W_{\text{pt,ref}}. \tag{26}$$

This assumes that the rest of the airframe is not significantly affected by incorporating a HEP or DP system. The accuracy of this assumption is debatable, but more detail would imply going to a complete Class-II weight estimation, which is not the objective of this method. The empirical correlations used in this paper for the wing, powertrain and operating empty weight of conventional aircraft are based on the books of Torenbeek [26] and Roskam [28]. Both $W_{\text{w,ref}}$ and W_{w} are estimated using the same correlation, but using different wing-loading values. The wing-loading value used to compute $W_{\text{w,ref}}$ can be estimated by calculating the maximum wing loading in absence of aero-propulsive interaction effects, i.e. $(W/S)_{\text{ref}} = q_\infty C_{L_{\text{max,airframe}}}$.

Finally, the weight of the powertrain has to be estimated. If the specific power (kW/kg) of each component of the corresponding powertrain architecture is known, then the complete powertrain weight can be estimated for a given MTOW value, since the power required from each component is determined by its respective power-loading diagram. For simplicity, the designer may choose to neglect the weight of some of the components in first instance. As discussed in Sec. II.B, it should be kept in mind that the weight of the converters and inverters of the system must be included in the specific powers assumed for the PMAD or electrical machines.

Since most of the component weights mentioned so far depend on the MTOW of the aircraft, an iterative calculation is required. After converging on the MTOW in the weight estimation module, the mission analysis can be employed to recompute the fuel and battery energy requirements, repeating the process until converging on a final MTOW value. Given that the current method neglects several potential weight benefits (wing bending relief, smaller high-lift systems, removal of auxiliary power units,...) and penalties (cooling systems[¶], cables,...) associated to HEDP systems, additional validation is required to verify the accuracy of the approach. In order to obtain a first estimate of the MTOW values calculated using the proposed method, Sec. III compares two HEDP concepts with a conventional reference aircraft.

III. Demonstration: Leading-Edge Distributed-Propulsion Configurations

The derivations presented so far are applicable to HEP aircraft with generic propulsion-system layouts. This section demonstrates how the method can be applied to tube-and-wing aircraft featuring leading-edge distributed-propulsion systems, similar to Concept 1 of Fig. 2. First, the aero-propulsive interaction model used to determine the "Delta" terms for such configurations is presented in Sec. III.A. Then, a set of hypothetical top-level requirements is defined in Sec. III.B, together with the assumed aircraft characteristics and design parameters. Finally, in Sec. III.C the results for three different powertrain architectures are compared.

A. Aero-Propulsive Interaction Model

As discussed in Sec. II.A.1, a series of "Delta" terms (ΔC_L, ΔC_{D_0}, ΔC_{D_i}, and $\Delta \eta_{\text{dp}}$) must be estimated in order to incorporate the aero-propulsive interaction effects in the design process. A preliminary method for wing leading-edge mounted, distributed tractor-propellers is proposed in this section. It is worth highlighting that the design procedure is also applicable to other novel propulsion-system layouts if the corresponding "Delta" models are determined.

[¶] The power dissipated in each powertrain component can easily be obtained from the powertrain model by subtracting the output power of each element from its input power. Therefore, the weight of the cooling system could be estimated if the correlation between the mass and the heat load of the system is known. The findings of previous studies [15] suggest that the thermal management system is one of the most important components to add to the proposed weight breakdown, especially for large aircraft.

1. Geometrical Description of the DP System

Before evaluating the Delta terms of Eqs. 2, 3 and 4, a simplified geometrical description of the system is required, as shown in Fig. 8. This simplified representation assumes that the wing has a rectangular planform of span b and chord c, and that the propulsors are not located near the wing root or tip. The DP system is considered to be an array of N propulsors of diameter D_p ($N/2$ propulsors per semi-wing, where N is equal to N_1 or N_2 depending on whether the DP system corresponds to the primary or secondary powertrain, respectively), aligned in spanwise direction with a separation $\delta_y D_\mathrm{p}$. A lateral clearance of $\delta_y/2$ is supposed at each end of the array, and the propulsors are positioned at an angle α_p relative to the freestream velocity vector. For a given number of propulsors and fraction of wingspan occupied by the DP array ($\Delta y/b$), the diameter of the propulsors can be computed as

$$D_\mathrm{p} = \frac{b \cdot (\Delta y/b)}{N(1+\delta_y)}. \tag{27}$$

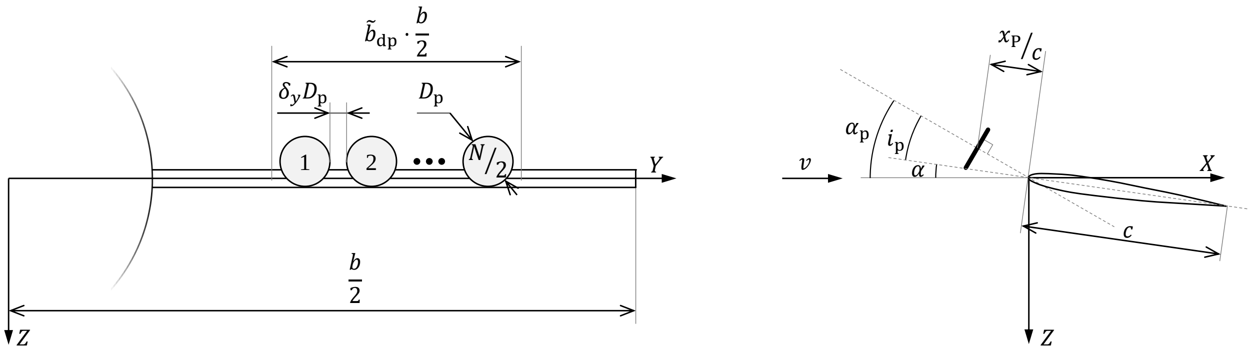

Fig. 8 Simplified DP-system representation, indicating the main geometrical parameters.

In Eq. 27, N and ($\Delta y/b$) are selected as design variables, while the diameter of the propulsors is selected as dependent variable. Although this does not necessarily have to be the case, this approach is preferred since the performance of the wing will strongly depend on the span fraction covered by the DP array. Moreover, the span interval along which propulsors are installed can be limited by structural constraints or the presence of the fuselage. Since the extensive parameter $b = \sqrt{SA}$ of Eq. 27 is unknown in the preliminary sizing process, the propulsor diameter is expressed in a normalized manner as

$$\frac{D_\mathrm{p}^2}{W} = \frac{(\Delta y/b)^2}{N^2\left(1+\delta_y\right)^2}\frac{A}{(W/S)}, \tag{28}$$

hereby defining a parameter which indicates how much propulsor-disk area is needed per unit of aircraft weight W, as a function of geometrical parameters and the wing loading of the aircraft, W/S. This parameter has units of m^2/N, and can therefore be interpreted as a weight-oriented disk loading. When selecting or analyzing different geometrical design parameters of the DP system, it is recommendable to verify that the disk-loading values obtained are feasible. If a large number of propulsors is selected for a small span interval and the required thrust-to-weight ratio of the design is high, the thrust required from the propulsors may be impossible to produce in practice. The thrust required from a single propulsor can be expressed as a non-dimensional thrust coefficient through

$$T_\mathrm{c} = \frac{1}{N}\frac{\chi(T/W)}{\rho v^2 (D_\mathrm{p}^2/W)}, \tag{29}$$

where v and ρ are the velocity and density of the freestream respectively. Although in this configuration the freestream velocity v perceived by the propulsors is approximately equal in magnitude to the flight speed V, different symbols are used to distinguish between the inflow velocity relative to the propulsors, and the velocity of the aircraft in an inertial reference frame. The easiest way to verify that the thrust coefficient obtained from the design point does not exceed a maximum specified value $T_\mathrm{c,max}$ is to plot a constraint line $W_\mathrm{TO}/P_\mathrm{p} = f(W_\mathrm{TO}/S, T_\mathrm{c,max})$ in the propulsive power-loading diagram for each constraint or flight condition using Eq. 29. Contrary to the performance constraints, this additional constraint imposes a lower bound on the feasible power-loading values.

2. *Estimation of* ΔC_L *and* ΔC_{D_i}

The method proposed in this section is based on the approach of Patterson and German [48]. It represents the propellers as actuator disks and the wing as a flat plate, incorporating a semi-empirical correction for finite slipstream height. The model includes several assumptions worth highlighting:

- The velocity increase at the actuator disk is computed assuming uniform axial inflow.
- Variations in lift due to swirl are neglected (actuator disk assumption).
- The flow over the wing is attached.
- The airfoil is symmetric, and thus zero lift is produced at $\alpha = 0$.
- The effect of each propeller on the adjacent ones is neglected.
- The effect of the propellers on the wing is limited to the spanwise interval occupied by the disks ($\Delta y/b$).
- Within this spanwise interval, the effect on the wing is considered uniform in spanwise direction. This assumption is more accurate if $\delta_y \ll 1$.
- The wing is supposed to be fully immersed in the slipstream, that is, half of the slipstream flows under the wing and half over the wing.

Due to these strong simplifications, the accuracy of this approach requires further investigation. This is especially the case in high-lift conditions or at high propeller incidence angles, since the stall behavior of the wing is not taken into account. Nonetheless, its simplicity and sensitivity to top-level design parameters make it suitable for the conceptual sizing phase.

The first step is to compute the axial induction factor at the propeller disk (a_p) as a function of the thrust-to-weight ratio of an individual propeller, $T_\mathrm{p}/W = \chi(T/W)/N$, and the disk loading defined in Eq. 28. This can be estimated using actuator disk theory [31]:

$$a_\mathrm{p} = \frac{\Delta v_\mathrm{p}}{v} = \frac{1}{2}\left(\sqrt{1 + \frac{8}{\rho\pi}\frac{(T_\mathrm{p}/W)}{(D_\mathrm{p}^2/W)}} - 1\right), \tag{30}$$

where Δv_p is the velocity increase at the propeller disk. Due to contraction, the slipstream velocity at the quarter chord[‖] of the wing will be higher than at the propeller disk (for tractor configurations). In order to evaluate the velocity induced by the propellers at the quarter-chord location, it is necessary to express the axial position of the propeller as a fraction of its radius:

$$\frac{x'_\mathrm{p}}{R_\mathrm{p}} = \frac{(x_\mathrm{p}/c) + 1/4}{(R_\mathrm{p}/c)}, \tag{31}$$

where the ratio between the propeller radius and the wing chord R_p/c can be computed using:

$$\frac{R_\mathrm{p}}{c} = \frac{1}{2}\sqrt{\left(\frac{D_\mathrm{p}^2}{W}\right)\left(\frac{W}{S}\right)A}. \tag{32}$$

It is now possible to compute the contraction ratio of the slipstream at the wing ($R_{c/4}/R_\mathrm{p}$) using:

$$\frac{R_{c/4}}{R_\mathrm{p}} = \sqrt{\frac{1 + a}{1 + a\left(1 + \frac{x'_\mathrm{p}/R_\mathrm{p}}{\sqrt{(x'_\mathrm{p}/R_\mathrm{p})^2 + 1}}\right)}}. \tag{33}$$

Finally, from conservation of mass in incompressible flow it follows that:

$$a_{c/4} = \frac{a}{(R_{c/4}/R_\mathrm{p})^2}. \tag{34}$$

[‖] The 2D Kutta-Joukowski theorem states that $l = \rho v \Gamma$, where l is the 2D lift of the airfoil section, Γ the circulation of an elementary vortex located at its quarter chord, and v the inflow velocity perceived by the vortex. Patterson and German [48] neglect slipstream contraction and use the induced velocity at the propeller disk to compute the lift on the wing. For the present paper, it was deemed more accurate to use the velocity at the quarter chord, even though this may lead to minor inconsistencies in the surrogate model used to determine the finite-slipstream correction factor β.

With this, the velocity increase due to the thrust generated by the propellers at the wing quarter chord is known. Following the derivation of Patterson and German [48] and modifying their equation to remove the singularity at $c_l = 0$, one can compute the sectional lift coefficient increase as:

$$\Delta c_l = 2\pi \left[\left(\sin\alpha - a_{c/4}\beta \sin i_\mathrm{p} \right) \sqrt{(a_{c/4}\beta)^2 + 2a_{c/4}\beta \cos(\alpha + i_\mathrm{p}) + 1} - \sin\alpha \right], \tag{35}$$

where α is the geometric angle of attack of the wing, i_p is the angle between the propeller axis and the wing chord (i.e. $i_\mathrm{p} = \alpha_\mathrm{p} - \alpha$), and β is a finite-slipstream correction factor. Since in the sizing process the angle of attack of the wing is unknown, it has to be estimated using the three-dimensional lift coefficient. This can be approximated by [49]:

$$\alpha \approx \frac{C_{L_\mathrm{airframe}}}{2\pi A} \left[2 + \sqrt{A^2(1 - M^2)\left(1 + \frac{\tan^2 \Lambda_{c/2}}{1 - M^2}\right) + 4} \right], \tag{36}$$

In Eq. 36, M is the freestream Mach number and $\Lambda_{c/2}$ the wing half-chord sweep angle. Since the aero-propulsive model assumes a rectangular wing, in this case the sweep angle is $\Lambda_{c/2} = 0$.

Determining the finite-slipstream correction factor β is a critical step in the process. If this term is neglected, the lift increase can be significantly over-estimated, especially for small ratios between the slipstream radius and wing chord [50]—as is the case for distributed propulsion. To this end, Patterson [25] generated a surrogate model based on CFD simulations of an actuator disk in front of a two-dimensional wing with a modified NACA 0012 airfoil. The surrogate model is used in this paper to compute β as a function of a_p, x_p/c, and R_p/c. It is worth noting that this surrogate model uses the induced velocity far downstream of the disk "V_j" as input, which according to the actuator disk theory is equal to $(1 + 2a_\mathrm{p})v$.

With the lift coefficient increase obtained from Eq. 35, the drag increase can be computed. The drag-coefficient increase due to thrust can be divided into two contributions:

$$\Delta c_d = \Delta c_{d_0} + \Delta c_{d_\mathrm{i}}. \tag{37}$$

The first term on the right-hand side of Eq. 37 represents the increase in friction drag on the wing surface due to increased dynamic pressure in the slipstream, and can therefore be computed using:

$$\Delta c_{d_0} = a_{c/4}^2 c_\mathrm{f}, \tag{38}$$

where c_f is the sectional skin friction coefficient, for which a value of 0.009 is assumed [51]. Since at this stage of the design process not enough information is available to obtain a meaningful estimation of the increase in wetted area due to pylons and nacelles, their contribution to Δc_{d_0} is neglected. The second term of the right-hand side of Eq. 37 represents the change in lift-induced drag of the wing due to the propeller-induced lift. This term could essentially be included in the drag polar by modifying the Oswald factor, as preferred by some authors [36]. However, given the difficulty of obtaining an accurate estimation of the Oswald factor for a generic aspect ratio, this term is approximated by [51]:

$$\Delta c_{d_\mathrm{i}} \approx \frac{2 C_{L_\mathrm{airframe}} \Delta c_l}{\pi A}. \tag{39}$$

The lift and drag coefficients obtained are sectional (i.e., two-dimensional) coefficients, averaged in spanwise direction within the interval occupied by the DP array. Assuming the effect of the propellers on the wing is limited to the spanwise interval they occupy, the three-dimensional coefficients can be related to the corresponding average sectional coefficients through:

$$\Delta C_L = \frac{\Delta c_l}{\Delta y/b}, \tag{40a}$$

$$\Delta C_{D_0} = \frac{\Delta c_{d_0}}{\Delta y/b}, \tag{40b}$$

$$\Delta C_{D_\mathrm{i}} = \frac{\Delta c_{d_\mathrm{i}}}{\Delta y/b}. \tag{40c}$$

Finally, the effect of the wing on the propellers is neglected, and thus $\Delta\eta_\mathrm{dp} = 0$. Although this term is actually non-zero [31], this approximation is considered accurate enough here since the effect of the wing on propeller performance is relatively small, especially when compared to other wing-mounted distributed-propulsion layouts such as over-the-wing propellers [52].

B. Top-Level Requirements and Assumptions

A regional transport aircraft comparable to the ATR 72-600 is considered, with a harmonic range of R = 825 nautical miles and a payload of W_{PL} = 73.6 kN. The aircraft has a cruise speed of M_{cr} = 0.41 at a cruise altitude of 18,000 ft, and the approach speed must be no greater than 115 kts. In the case of a balked landing (BL), the aircraft must be able to attain a climb gradient of 2.1% at 1.4 times the reference stall speed V_{SR} with one engine inoperative [53]. Furthermore, a diversion range of 100 nm is required, for which a diversion altitude and Mach number of 10,000 ft and 0.3 are assumed, respectively. Finally, the aircraft must be able to take off with a field length of less than 1333 m. These aircraft requirements are collected in Table 3. The design parameters selected to meet these requirements are given in Table 4. Several of the values shown in these tables are based on ATR 72-600 reference data [54]. Three powertrain architectures are examined as candidates: conventional (Fig. 6.1), serial (Fig. 6.3), and partial-turboelectric (PTE, Fig. 6.5).

Table 3 Top-level aircraft requirements.

Parameter	Value
Payload, W_{PL} [kN]	73.6
Cruise altitude, h_{cr} [ft]	18,000
Cruise Mach number, M_{cr} [-]	0.41
Range, R [nm]	825
Approach speed, V_{app} [kts]	115
OEI BL climb gradient, c_{BL} [%]	2.1
OEI BL climb speed, V_{BL} [kts]	$1.4V_{\mathrm{SR}}$
Diversion altitude, h_{div} [ft]	10,000
Diversion Mach number, M_{div} [-]	0.3
Diversion range, R_{div} [nm]	100
Take-off field length, S_{TO} [m]	1333

Table 4 Selected design parameter values. Asterisks indicate parameters which are only applicable to the hybrid-electric concepts.

Parameter	Value
Aspect ratio, A [-]	12
Half-chord sweep, $\Lambda_{c/2}$ [deg]	0
Taper ratio [-]	0.62
Root thickness-to-chord ratio [-]	0.18
N° of primary propulsors, N_1 [-]	2
N° of secondary propulsors*, N_2 [-]	12
DP span fraction*, $\Delta y/b$ [-]	0.6
Spacing between DP propulsors*, δ_y [-]	0.01
Axial position of DP propulsors*, x_{p}/c [-]	0.2

In order to perform the preliminary sizing of the aircraft, a series of parameter values have to be assumed with respect to the aircraft technology. Several parameters related to the hybrid-electric powertrain are gathered in Table 5. The parameters which depend on the aircraft configuration (clean, take-off, or landing), on the other hand, are shown in Table 6. These parameters are presented per performance constraint. For all three design concepts, no thrust vectoring is considered, i.e. $\alpha_{\mathrm{p}} = 0$. Furthermore, the weights of the gearbox, PMAD and propulsors are neglected. The efficiency and specific power of the electrical machines are based on the technology goals presented in Ref. [9], and include both the electrical machine itself and the associated inverter. For the batteries, a specific energy of 500 Wh/kg at pack level is selected, which is considered an optimistic value for the 2035 time frame, close to the theoretical limits of lithium-ion batteries at cell level [14, 55, 56]. Moreover, a specific power of 1 kW/kg is assumed at pack level.

Table 5 Assumed HEP technology levels.

Parameter	Value	Parameter	Value
Battery pack specific energy, e_{bat} [Wh/kg]	500	EM efficiency (η_{EM1} or η_{EM2}) [-]	0.96
Battery pack specific power [kW/kg]	1	PMAD efficiency, η_{PM} [-]	0.99
Minimum SOC [%]	20	Gearbox efficiency, η_{GB} [-]	0.96
EM specific power [kW/kg]	7.7	Gas turbine efficiency, η_{GT} [-]	0.3

In order to size the aircraft for energy requirements, a mission profile is defined and shown in Fig. 9. In this simplified mission, the climb, cruise, and descent phases are analyzed for both the nominal mission and the diversion. Since the main focus of the mission analysis is to determine energy consumption, the take-off and landing segments are neglected. During climb, all power-control parameters are specified as input, and the corresponding acceleration and climb rate are computed. During cruise, the flight condition is completely specified in terms of speed and altitude, and thus one control parameter less can be used as input. The control parameters selected as input depend on the powertrain architecture considered. For the descent phase, all power-control laws are specified, while the descent rate and deceleration are subsequently calculated. Finally, for the diversion part of the mission, the same strategy is followed as for the nominal mission, though at different altitudes and velocities. The power-control profiles which are used are presented in Sec. III.C in tandem with those obtained for the mission segments for which they are not predefined.

Table 6 Assumed aerodynamic and mission properties per constraint. All parameters are non-dimensional. Asterisks indicate parameters which are only applicable to the hybrid-electric concepts. The supplied power ratio and shaft power ratio values are applied to the serial and PTE powertrain architectures respectively.

	Cruise speed	**Approach speed**	**Take-off distance**	**OEI climb gradient**
Flap configuration	clean	landing	take-off	landing
Landing gear position	retracted	extended	extended	retracted
Zero-lift drag coefficient, C_{D_0}	0.02	0.085	0.035	0.65
Oswald factor, e	0.85	1.00	0.95	1.00
Maximum lift coefficient, $C_{L_{\text{max,airframe}}}$	-	2.8	2.2	2.8
Propulsive efficiency (primary), η_{p1}	0.9	0.8	0.75	0.8
Propulsive efficiency (secondary)*, η_{p2}	0.85	0.75	0.7	0.75
Aircraft weight fraction, f_W	0.98	0.95	1	0.95
Gas turbine throttle, ξ_{GT}	0.8	0.5	1	1
Supplied power ratio*, Φ	0.05	0	0.1	0.1
Shaft power ratio*, φ	0.9	0.7	0.7	0.5

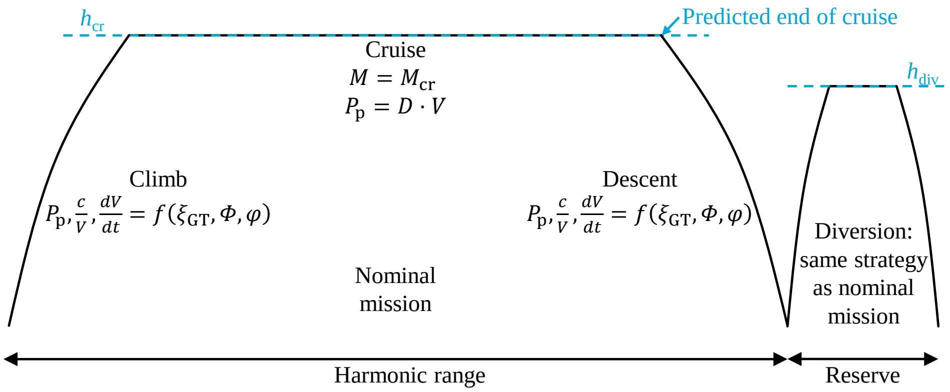

Fig. 9 Simplified mission profile used for computing the energy consumption in the mission analysis.

C. Results

The power-loading diagrams obtained for the three different powertrain architectures are shown in Fig. 10. For the conventional architecture (Fig. 10a), only the gas-turbine power-loading diagram is presented, while for the serial and PTE architectures (Fig. 10b and Fig. 10c, respectively) the secondary electrical-machine power-loading has been included for comparison. For the constraints and HEP architectures considered here, the secondary electrical machines act as electromotors, powering the propulsors of the DP system. Furthermore, for the serial architecture, the battery power-loading diagram has been included. Note that the battery power-loading plot has different y-axis limits. Given the sensitivity of MTOW to battery specific energy [10, 14, 19, 21] and the assumed technology levels, higher battery power-loading values are required to avoid an excessively high MTOW.

The increase in maximum wing loading due to DP is evident in Fig. 10. For the conventional architecture, which corresponds to a twin-engine turboprop aircraft, no aero-propulsive effects have been included. In this way, the diagram of Fig. 10a can be compared with the reference aircraft, and the effect of including the aero-propulsive interaction in the sizing process can be distinguished. However, in practice, this configuration also presents appreciable interaction effects between the propeller and the wing. Thus, the actual increase in wing loading due to DP is slightly lower than suggested by Fig. 10. The increase in wing loading is higher for the serial architecture than for the PTE architecture, since for the latter the shaft power ratio is $\varphi = 0.7$ in landing conditions (see Table 6), and thus not all the power is used to enhance lift. For the PTE architecture a shaft power ratio lower than unity was selected in landing conditions because, for the aerodynamic characteristics assumed, using all thrust to enhance lift in landing conditions leads to an excessively high wing-loading, with a negative impact on cruise performance. In practice this would imply that a smaller, less complex high-lift system could be used during landing, compensating the decrease in $C_{L_{\mathrm{max,airframe}}}$ by increasing the shaft power ratio. In any case, this effect highlights the versatility of the PTE architecture in terms of power distribution.

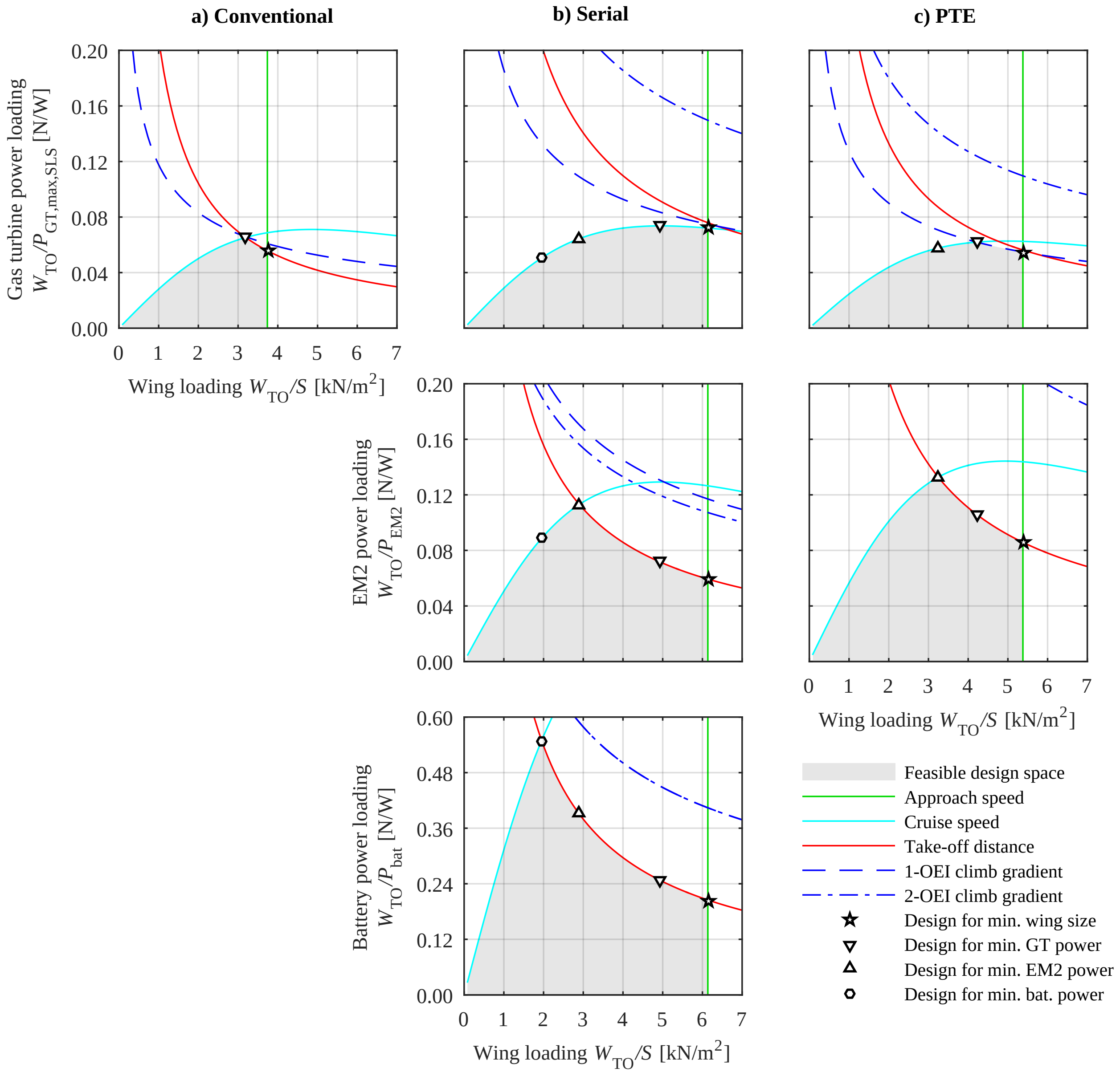

Fig. 10 Component power-loading diagrams for the (a) conventional, (b) serial, and (c) PTE powertrain architectures. Configurations (b) and (c) have a distributed propulsion system, while for configuration (a) no aero-propulsive effects are considered. The OEI climb gradient is evaluated in landing configuration, with "1-OEI" and "2-OEI" indicating failure of a component of the primary and secondary powertrain branches, respectively.

The topmost plot of Fig. 10b shows that the gas-turbine power-loading of the serial architecture is higher than the conventional one. Moreover, the gas turbine is sized by the cruise constraint, rather than the take-off constraint. This is a result of the battery-assisted take-off. As a consequence, the gas turbine operates near its design condition for a large part of the mission. This can lead to a benefit in gas turbine efficiency η_{GT} [43, 57], although this effect has not been included here. For the PTE architecture, on the other hand, the gas turbine is sized at max wing loading by the climb-gradient constraint during component failure in the primary powertrain branch. For the gas turbine, the constraint line corresponding to a failure in the secondary powertrain branch is equal to the constraint line that would be obtained without component failure, since a failure in the secondary powertrain branch does not affect the gas turbine (see Sec. II.B.5). When comparing the two plots of Fig. 10c, one can observe that a failure in the primary powertrain branch requires the components of that branch to be over-sized by a factor 2, while a failure in the secondary powertrain branch only requires the corresponding components to be over-sized by a factor 12/11. For that reason, the “OEI” constraints are not limiting in the secondary electrical-machine power-loading diagrams. Figure 10 shows that these components are limited by the take-off constraint for both the serial and the PTE architectures. However, a higher power-loading is achieved for the latter, since during take-off part of the propulsive power is generated by the primary propulsors.

Different design points are included in Fig. 10. These show how the optimum design point in terms of one component generally does not coincide with the optimum size of other components. In this paper, the design point for maximum wing loading is selected, which usually corresponds to the smallest wing size. However, this is not necessarily the case. Due to the large impact of the powertrain on MTOW, it may be more beneficial to select one of the other design points, or even a different combination of wing loading and power loading that minimizes MTOW or another figure of merit. This can lead to increased component power-loading, and therefore reduced powertrain weight—assuming that the reduction in powertrain mass is not outweighed by the increase in wing mass. Furthermore, when the aero-propulsive effects in landing conditions lead to an excessively high maximum wing loading, the resulting lift coefficient required during cruise may be sub-optimal. In this case, selecting maximum wing loading as design criterion leads to lift-coefficient values in cruise which are above the value corresponding to maximum lift-to-drag ratio, L/D.

The average cruise L/D can be obtained from the mission analysis. The power-control strategies used for the mission analysis are shown in Fig. 11. Thick lines indicate power-control profiles specified by the designer as input. The thin lines, on the other hand, are a result of applying the point model for a fixed flight condition. The six mission segments assumed in Fig. 9 are delimited by dotted lines. For the conventional architecture (Fig. 11a), constant throttle values are assumed during climb and descent, with the cruise throttle decreasing over time to compensate the reduction in aircraft weight. For the serial architecture (Fig. 11b), throttle is specified during cruise, while the supplied power ratio is adapted to compensate the changes in thrust requirements. This strategy aims to maximize the efficiency of the gas turbine throughout the mission, although the current method is not sensitive to this effect unless η_{GT} is adapted accordingly. In this case, the batteries provide a small amount of power during the beginning of cruise, while towards the end of

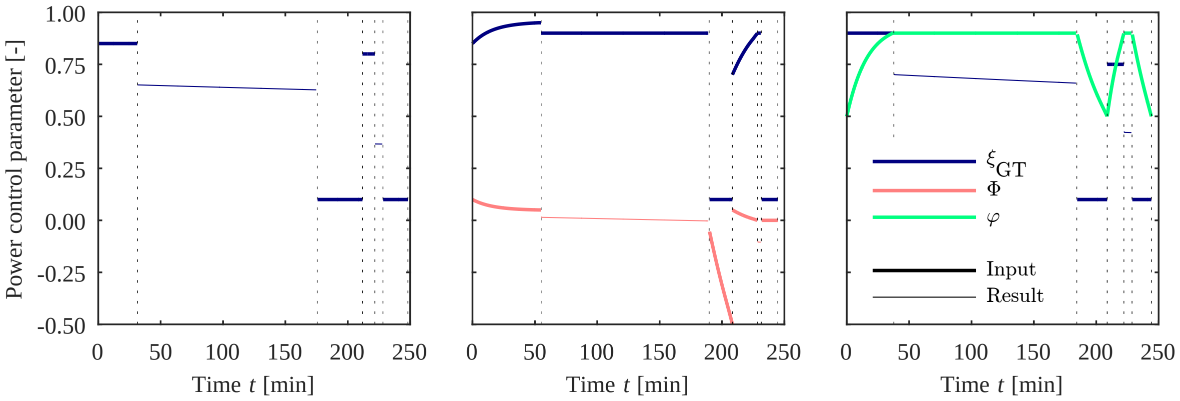

a) Conventional **b) Serial** **c) PTE**

Fig. 11 Power-control profiles of the three powertrain architectures considered. Dotted lines indicate, from left to right, the end of the climb, cruise, descent, diversion climb, diversion cruise, and diversion descent mission segments, respectively. Take-off and landing are not included.

cruise they are charged by the excess power produced by the gas turbine. During descent, a negative supplied power ratio is specified, such that the power produced by the gas turbine in idle conditions is used to recharge the batteries. This extra battery energy can be used for the diversion phase, or to reduce charging time on the ground. Finally, for the PTE architecture (Fig. 11c), a φ profile is specified throughout the mission in order to maximize aero-propulsive performance, while the throttle is varied accordingly. In all three cases, the power-control parameters selected in the constraints diagram and the power-control profiles assumed in the mission analysis must be consistent. This does not imply, however, that the same ξ_{GT}, Φ, or φ are obtained in the mission analysis, since the components can be sized by different constraints in the power-loading diagram. For this reason, the cruise throttle values obtained in Fig. 11a and 11c do not coincide with the value specified in Table 6, for example.

Combining the power-loading diagrams with the mission analysis and weight estimation modules provides the take-off mass, wing area, and fuel and battery energy of the aircraft. Table 7 collects these parameters along with the design wing-loading and power-loading, as well as the average lift-to-drag ratio during the cruise phase. The conventional architecture compares well with the reference aircraft in terms of power-loading[**] and wing-loading, although the maximum take-off mass (MTOM) and fuel energy are slightly over- and under-estimated, respectively. This can be attributed to inaccuracies in the empirical weight correlations, or in the assumed aerodynamic and mission properties. Despite the higher wing-loading values obtained for the two HEP concepts, they are heavier than the conventional concept due to the increased powertrain weight. As expected, this is especially the case if batteries are included: the serial configuration is 33% heavier than the conventional configuration, while the PTE configuration is only 6% heavier. Nonetheless, the increased wing loading leads to a reduced wing size for both HEP concepts. The corresponding L/D increase is not large enough to offset the increase in aircraft weight, leading to increased block fuel consumption with respect to the conventional concept. The modest increase in L/D of the HEP concepts can be attributed to the conventional aircraft already operating near its maximum lift-to-drag ratio for the given mission, while the HEP concepts operate at higher, less optimal lift coefficients. This result highlights the importance of determining the optimal mission profiles for HEP concepts, for which they may exceed the performance of conventional layouts.

Table 7 Summary of results for the three configurations analyzed. ATR 72-600 data at max payload has been included for reference [54]. Lift-to-drag ratio is presented as cruise-phase average.

	Reference	Conventional	Serial	PTE
Gas turbine power loading, $W_{\mathrm{TO}}/P_{\mathrm{GT,max,SLS}}$ [N/W]	0.058	0.056	0.072	0.055
Wing loading, W_{TO}/S [kN/m^2]	3.67	3.74	6.14	5.38
Maximum take-off mass, MTOM [t]	22.8	23.7	31.6	25.3
Wing area, S [m^2]	61	62	50	46
Fuel energy, E_{f} [GJ]	85.6	78.7	117.1	96.4
Battery energy, E_{bat} [GJ]	0	0	3.3	0
Cruise lift-to-drag ratio, $(L/D)_{\mathrm{cr}}$ [-]	-	19.3	19.9	20.2

The differences in MTOM of the three concepts are further clarified in the breakdowns presented in Fig. 12. With the proposed weight breakdown, the operating empty mass excluding wing and powertrain (OEM') is comparable for the three aircraft. However, the wing mass fraction is lower for the two HEP concepts, due to the increased wing loading. Figure 12 also shows that not only the fuel mass, but also the fuel fraction is slightly higher for the HEP concepts than for the conventional concept. This indicates that, for the given mission, the increase in L/D does not offset the lower propulsive efficiency assumed for the DP system (see Table 6) and the power lost in the conversion from mechanical energy to electrical energy and vice versa.

Figure 12 also shows that the total powertrain weight fractions of the serial (7.4%) and PTE (8.0%) architectures exceed the weight fraction of the conventional one (4.8%). Although in the serial architecture the gas-turbine weight fraction is reduced, this does not compensate the increase in weight due to the electrical components. The reduction in gas-turbine weight fraction can be attributed to several reasons. Firstly, the relative impact of the gas turbine on the total aircraft weight is reduced due to the appearance of additional weight contributions. Secondly, the aero-propulsive benefit enabled by the HEP powertrain leads to an increased gas-turbine power-loading at the design point. Moreover, in the case of a serial architecture, the addition of battery power during take-off also allows for an increased gas-turbine

---

[**] Since the reference data provides P_{s1} instead of P_{gt}, the reference power-loading has been multiplied by η_{GB} in order to compare $W_{\mathrm{TO}}/P_{\mathrm{GT,max,SLS}}$ in equal conditions.

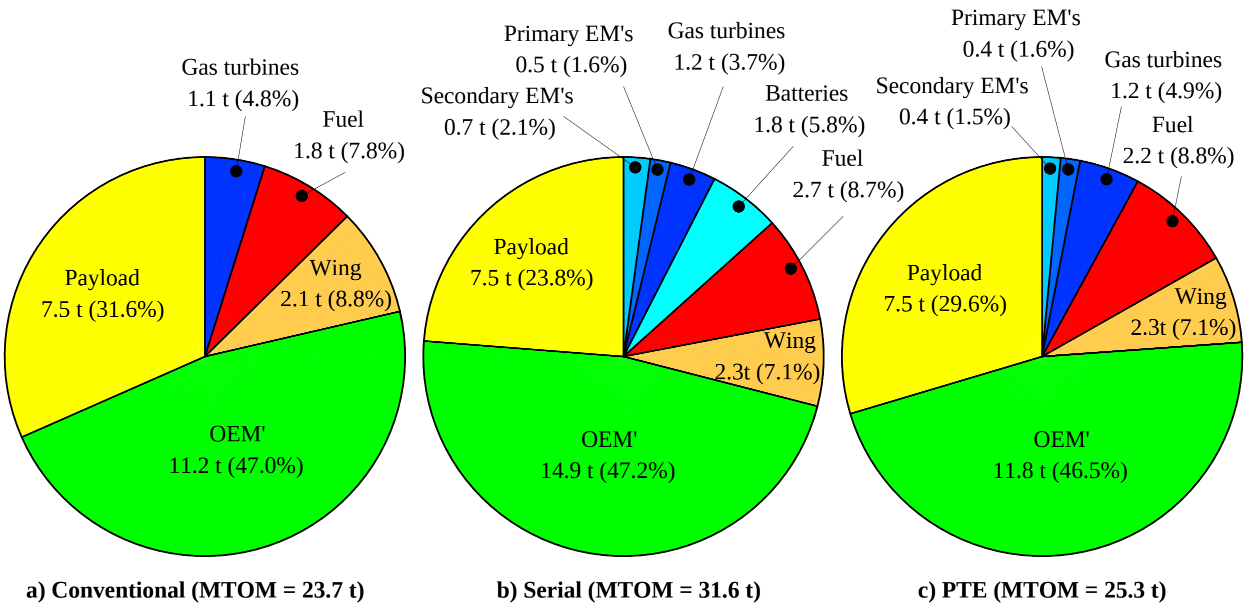

Fig. 12 Mass breakdown of the three configurations evaluated. Values are expressed in metric tons and as a percentage of maximum take-off mass. OEM' refers to the operating empty mass excluding wing and powertrain.

power-loading. The effect is clearly visible in Fig. 13. This figure shows the power flows across the three architectures, including a visual representation of the external layout for clarity. The results are presented in take-off conditions, which is the sizing condition for most components (see Fig. 10). Despite the significantly higher MTOW of the serial concept, the power produced by the gas turbine P_{gt} is comparable to the other two concepts. This is attributed to the relatively small, yet efficient, contribution of the batteries. However, since all power has to be diverted to the secondary propulsors, the power produced by the electrical machines is higher for the serial architecture than for the PTE architecture. Consequently, the weight fraction of the electrical machines is higher for the serial architecture, as reflected in Fig. 12.

The results indicate that the two HEP concepts present no benefit with respect to a conventional powertrain. This is in line with the findings of previous studies, which show that either more optimistic e_{bat} values [9, 14, 21, 45] or reduced ranges [8, 16–18, 24] are required for the HEP concepts to be competitive. Nonetheless, the results demonstrate the versatility of the method and provide valuable insight into possible areas of improvement. Firstly, the power-loading diagrams show which performance requirements are constraining for each component of each powertrain architecture, clearly indicating in which flight condition the aerodynamic or operational characteristics must be improved in order to obtain a benefit at aircraft level. Secondly, the use of two energy sources provides a degree of freedom which allows maximizing the performance of the powertrain, while the use of two propulsion systems provides a degree of freedom which allows maximizing the aerodynamic performance of the aircraft. Thus, the more advanced powertrain layouts (e.g., the SPPH) should not be discarded a priori due to their complexity or weight penalty, since they can be used in a much more beneficial manner throughout the mission. Thirdly, before analyzing the optimal HEP or DP configuration for a given mission, it is interesting to analyze for which mission these concepts can present a benefit with respect to conventional powertrains in the first place. For example, the increased lift-to-drag ratio enabled by DP systems confirms that higher harmonic ranges must be evaluated, such that the benefit in aero-propulsive efficiency can lead to a fuel weight reduction which offsets the powertrain weight penalty. Moreover, the sub-optimal lift coefficients attained with excessively high wing-loading values indicate that different altitudes and speeds should be evaluated, such that the wing area can be minimized while maintaining an optimum lift coefficient during cruise. In order to do so, the proposed method is capable of rapidly[††] evaluating different combinations of mission requirements, powertrain architecture, propulsion-system layout, and assumed technology levels. Finally, the method can also be used in sensitivity or optimization studies to determine more optimal power-control profiles and design-parameter values for the DP system.

[††] In this study, the complete preliminary sizing routine including aero-propulsive effects required approximately 15 seconds on a single core.

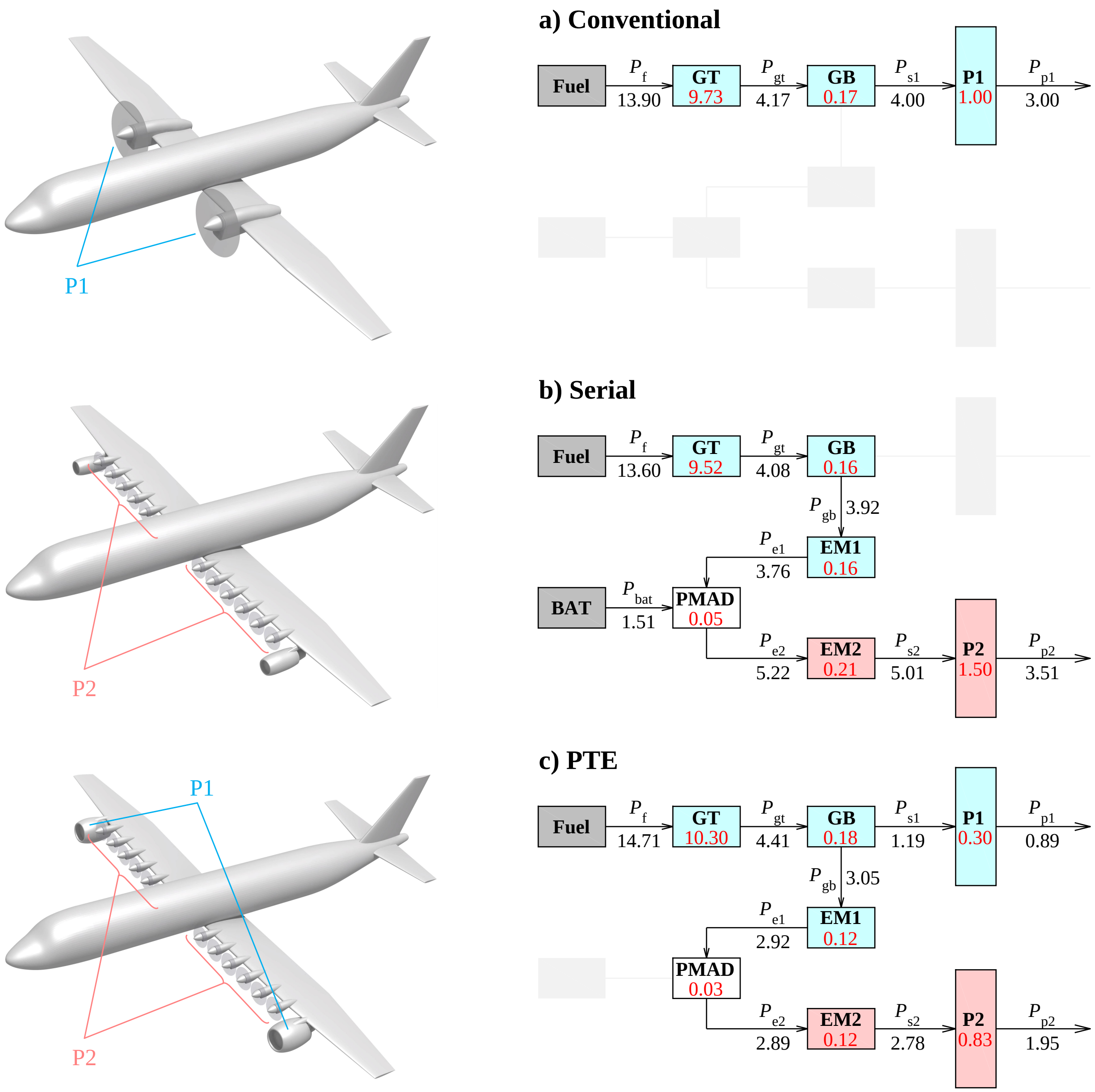

Fig. 13 Visual representation of the external layout (left) and powertrain architecture (right) of the three concepts evaluated. Values inside the component boxes indicate the power losses in that element. All values are presented in MW for take-off conditions.

IV. Conclusions & Outlook

A preliminary sizing method has been described which determines the wing area, installed power, and maximum take-off weight of a generic hybrid-electric aircraft configuration. To this end, a simplified powertrain model has been proposed, and a method to estimate the aero-propulsive interaction effects for leading-edge-mounted distributed-propulsion (DP) systems has been presented. These models have subsequently been applied to a regional transport aircraft. The results of this demonstration case confirm that, for the assumed technology levels and mission requirements, the use of hybrid-electric distributed propulsion (HEDP) does not lead to any benefit at aircraft level when compared to a conventional powertrain. The HEDP concept featuring a serial powertrain architecture is 33% heavier than a conventional configuration, while the concept featuring a partial turboelectric (PTE) architecture is 6% heavier. However, these results have been obtained without any systematic sensitivity or optimization studies. Moreover, since the method is flexible and sensitive to the relevant top-level design parameters, it can easily be applied to evaluate other configurations and requirements. More specifically, the findings indicate that a PTE architecture or a serial/parallel partial hybrid (SPPH) architecture with a limited amount of batteries can be promising when combined with DP for longer ranges. Furthermore, the results reaffirm that the mission and power-control profiles have a significant influence on the resulting aircraft characteristics, and that the proposed method is capable of analyzing their impact early in the design process.

This method provides quick and visually-evident way of relating the findings of higher-fidelity propulsion-system studies to their impact at aircraft level. Nevertheless, in terms of the method itself, multiple improvements can be incorporated. Most importantly, the powertrain model can be improved by, for example, incorporating the effect of battery state-of-charge, variable gas-turbine efficiency, and the thermal management system. Regarding the aero-propulsive interaction model, accurate high-lift performance predictions are required. Such a model should also be developed for different propulsion system layouts in a non-dimensional or normalized manner, based on detailed aerodynamic studies. For this reason, future work will focus on incorporating a model for over-the-wing DP systems in the design loop. The implementation of different aero-propulsive models will broaden the applicability of the method and enable the rapid design-space exploration of a wide range of aircraft configurations.

Acknowledgments

This research is part of the European Union's Clean Sky 2 Large Passenger Aircraft program (CS2-LPA-GAM-2014-2015-01). The authors would like to thank the other partners of LPA WP1.6 and the NOVAIR project participants for their valuable feedback. Wing, tail, and fuselage CAD geometries were created based on reference aircraft data using Pacelab APD.

References

[1] Bonet, J. T., Schellenger, H. G., Rawdon, B. K., Elmer, K. R., Wakayama, S. R., Brown, D. L., and Guo, Y., "Environmentally Responsible Aviation (ERA) Project - N+2 Advanced Vehicle Concepts Study and Conceptual Design of Subscale Test Vehicle (STV): Final Report," Technical Report NASA/CR-2011-216519, December 2011.

[2] Advisory Council for Aviation Research and Innovation in Europe (ACARE), "Realising Europe's vision for aviation: Strategic research & innovation agenda, Vol. 1," Advisory Council for Aviation Research and Innovation in Europe, 2012.

[3] Borer, N. K., Patterson, M. D., Viken, J. K., Moore, M. D., Clarke, S., Redifer, M. E., Christie, R. J., Stoll, A. M., Dubois, A., Bevirt, J. B., Gibson, A. R., Foster, T. J., and Osterkamp, P. G., "Design and Performance of the NASA SCEPTOR Distributed Electric Propulsion Flight Demonstrator," 16th AIAA Aviation Technology, Integration, and Operations Conference, Washington, DC, USA, June 13-17 2016.

[4] Felder, J. L., Kim, H. D., and Brown, G. V., "Turboelectric Distributed Propulsion Engine Cycle Analysis for Hybrid-Wing-Body Aircraft," 47th AIAA Aerospace Sciences Meeting, Orlando, FL, USA, January 5-8 2009.

[5] Rothaar, P. M., Murphy, P. C., Bacon, B. J., Gregory, I. M., Grauer, J. A., Busan, R. C., and Croom, M. A., "NASA langley distributed propulsion VTOL tilt-wing aircraft testing, modeling, simulation, control, and flight test development," 14th AIAA Aviation Technology, Integration, and Operations Conference, Atlanta, GA, USA, June 16-20 2014.

[6] Schiltgen, B., Freeman, J. L., and Hall, D. W., "Aeropropulsive Interaction and Thermal System Integration within the ECO-150: A Turboelectric Distributed Propulsion Airliner with Conventional Electric Machines," 16th AIAA Aviation Technology, Integration and Operations Conference, Washington, DC, USA, June 13-17 2016.

[7] Hermetz, J., Ridel, M., and Döll, C., "Distributed electric propulsion for small business aircraft: A concept-plane for key-technologies investigations," 30th ICAS Congress, Daejeon, South Korea, 2016.

[8] Stoll, A. M., and Mikić, G. V., "Design Studies of Thin-Haul Commuter Aircraft with Distributed Electric Propulsion," 16th AIAA Aviation Technology, Integration, and Operations Conference, Washington, DC, USA, June 13-17 2016.

[9] Jansen, R. H., Bowman, C., Jankovsky, A., Dyson, R., and Felder, J., "Overview of NASA Electrified Aircraft Propulsion Research for Large Subsonic Transports," 53rd AIAA/SAE/ASEE Joint Propulsion Conference, Atlanta, GA, USA, July 10-12 2017.

[10] Sgueglia, A., Schmollgruber, P., Bartoli, N., Atinault, O., Benard, E., and Morlier, J., "Exploration and Sizing of a Large Passenger Aircraft with Distributed Ducted Electric Fans," 2018 AIAA Aerospace Sciences Meeting, Kissimmee, FL, USA, January 8-12 2018.

[11] Steiner, H. J., Seitz, A., Wieczorek, K., Plötner, K., Iskiveren, A. T., and Hornung, M., "Multi-disciplinary design and feasibility study of distributed propulsion systems," 28th ICAS Congress, Brisbane, Australia, September 23-28 2012.

[12] Gohardani, A. S., Doulgeris, G., and Singh, R., "Challenges of future aircraft propulsion: A review of distributed propulsion technology and its potential application for the all electric commercial aircraft," *Progress in Aerospace Sciences*, Vol. 47, 2011, pp. 369–391.

[13] Kim, H. D., "Distributed Propulsion Vehicles," 27th Congress of the International Council of the Aeronautical Sciences, Nice, France, September 19-24 2010.

[14] Voskuijl, M., van Bogaert, J., and Rao, A. G., "Analysis and design of hybrid electric regional turboprop aircraft," *CEAS Aeronautical Journal*, Vol. 9, 2018, pp. 15–25.

[15] Kim, J. H., Kwon, K. S., roy, S., Garcia, E., and Marvis, D., "Megawatt-class Turboelectric Distributed Propulsion, Power, and Thermal Systems for Aircraft," 2018 AIAA Aerospace Sciences Meeting, Kissimmee, FL, USA, January 8-12 2018.

[16] Antcliff, K. R., and Capristan, F. M., "Conceptual Design of the Parallel Electric-Gas Architecture with Synergistic Utilization Scheme (PEGASUS) Concept," 17th AIAA/ISSMO Multidisciplinary Analysis and Optimization Conference, Denver, CO, USA, June 5-9 2017.

[17] Wroblewski, G. E., and Ansell, P. J., "Mission Analysis and Emissions for Conventional and Hybrid-Electric Commercial Transport Aircraft," 2018 AIAA Aerospace Sciences Meeting, Kissimmee, FL, USA, January 8-12 2018.

[18] Dean, T. S., Wroblewski, G. E., and Ansell, P. J., "Mission Analysis and Component-Level Sensitivity Study of Hybrid-Electric General Aviation Propulsion Systems," 2018 AIAA Aerospace Sciences Meeting, Kissimmee, FL, USA, January 8-12 2018.

[19] Cinar, G., Mavris, D. N., Emeneth, M., Schneegans, A., Riediger, C., Fefermann, Y., and Isikveren, A. T., "Sizing, Integration and Performance Evaluation of Hybrid Electric Propulsion Subsystem Architectures," 55th AIAA Aerospace Sciences Meeting, Grapevine, TX, USA, January 9-13 2017.

[20] Isikveren, A. T., Kaiser, S., Pornet, C., and Vratny, P. C., "Pre-design strategies and sizing techniques for dual-energy aircraft," *Aircraft Engineering and Aerospace Technology: An International Journal*, Vol. 86(6), 2014, pp. 525–542.

[21] Pornet, C., and Isikveren, A. T., "Conceptual design of hybrid-electric transport aircraft," *Progress in Aerospace Sciences*, Vol. 79, 2015, pp. 114–135.

[22] Nam, T., Soban, D. S., and Mavris, D. N., "Power Based Sizing Method for Aircraft Consuming Unconventional Energy," 43rd AIAA Aerospace Sciences Meeting and Exhibit, Reno, NV, USA, January 10-13 2005.

[23] Perullo, C., and Mavris, D., "A review of hybrid-electric energy management and its inclusion in vehicle sizing," *Aircraft Engineering and Aerospace Technology: An International Journal*, Vol. 86(6), 2014, pp. 550–557.

[24] Kreimeier, M., and Stumpf, E., "Benefit evaluation of hybrid electric propulsion concepts for CS-23 aircraft," *CEAS Aeronautical Journal*, Vol. 8, 2017, pp. 691–704.

[25] Patterson, M. D., "Conceptual Design of High-Lift Propeller Systems for Small Electric Aircraft," PhD Dissertation, Georgia Institute of Technology, 2016.

[26] Torenbeek, E., *Synthesis of Subsonic Airplane Design*, Delft University Press, 1982.

[27] Mattingly, J. D., *Aircraft engine design*, AIAA Education Series, 2002.

[28] Roskam, J., *Airplane Design*, DARcorporation, 1985.

[29] Raymer, D. P., *Aircraft design: A conceptual approach*, AIAA Education Series, 2002.

[30] ESDU, "Thrust and drag accounting for propeller/airframe interaction," ESDU 85017, 1985.

[31] Veldhuis, L. L. M., "Propeller Wing Aerodynamic Interference," PhD Dissertation, Delft University of Technology, 2005.

[32] Smith Jr., L. H., "Wake Ingestion Propulsion Benefit," *Journal of Propulsion and Power*, Vol. 9(1), 1993, pp. 74–83.

[33] Seitz, A., and Gologan, C., "Parametric design studies for propulsive fuselage aircraft concepts," *CEAS Aeronautical Journal*, Vol. 6(1), 2015, pp. 69–82.

[34] Lv, P., Rao, A. G., Ragni, D., and Veldhuis, L., "Performance Analysis of Wake and Boundary-Layer Ingestion for Aircraft Design," *Journal of Aircraft*, Vol. 53(5), 2016, pp. 1517–1526.

[35] Mikić, G. V., Stoll, A. M., Bevirt, J., Grah, R., and Moore, M. D., "Fuselage Boundary Layer Ingestion Propulsion Applied to a Thin Haul Commuter Aircraft for Optimal Efficiency," 16th AIAA Aviation Technology, Integration, and Operations Conference, Washington, DC, USA, June 13-17 2016.

[36] Patterson, M. D., and Borer, N. B., "Approach Considerations in Aircraft with High-Lift Propeller Systems," 17th AIAA Aviation Technology, Integration, and Operations Conference, Denver, CO, USA, June 5-9 2017.

[37] Hooker, J. R., Wick, A., Zeune, C., and Agelastos, A., "Over Wing Nacelle Installations for Improved Energy Efficiency," 31st AIAA Applied Aerodynamics Conference, San Diego, CA, USA, June 24-27 2013.

[38] Cinar, G., Mavris, D. N., Emeneth, M., Schneegans, A., and Fefermann, Y., "Development of Parametric Power Generation and Distribution Subsystem Models at the Conceptual Aircraft Design Stage," 55th AIAA Aerospace Sciences Meeting, Grapevine, TX, USA, January 9-13 2017.

[39] Marwa, M., Martin, S. M., Martos, B. C., and Anderson, R. P., "Analytic and Numeric Forms for the Performance of Propeller-Powered Electric and Hybrid Aircraft," 55th AIAA Aerospace Sciences Meeting, Grapevine, TX, USA, January 9-13 2017.

[40] Jagannath, R., Bane, S. P. M., Nalim, M. R., and Javed Khan, M., "A Simplified Method To Calculate The Fuel Burn Of A Hybrid-Electric Airplane," 50th AIAA/ASME/SAE/ASEE Joint Propulsion Conference, Cleveland, OH, USA, July 28-30 2014.

[41] Felder, J. L., "NASA Electric Propulsion System Studies," EnergyTech 2015, Cleveland, OH, USA, November 30-December 2 2015.

[42] National Academies of Sciences, Engineering, and Medicine, *Commercial Aircraft Propulsion and Energy Systems Research: Reducing Global Carbon Emissions*, National Academies Press, 2016.

[43] Ang, A. W. X., Gangoli Rao, A., Kanakis, T., and Lammen, W., "Performance analysis of an electrically assisted propulsion system for a short-range civil aircraft," *Proceedings of the Institution of Mechanical Engineers, Part G: Journal of Aerospace Engineering*, 2018.

[44] Ruijgrok, G. J. J., *Elements of airplane performance*, Delft University Press, 1996.

[45] Isikveren, A. T., Pornet, C., Vratny, P. C., and Schmidt, M., "Optimization of Commercial Aircraft Using Battery-Based Voltaic-Joule/Brayton Propulsion," *Journal of Aircraft*, Vol. 54(1), 2017, pp. 246–261.

[46] Seitz, A., Bijewitz, J., Kaiser, S., and Wortmann, G., "Conceptual investigation of a propulsive fuselage aircraft layout," *Aircraft Engineering and Aerospace Technology: An International Journal*, Vol. 86(6), 2014, pp. 464–472.

[47] Vratny, P. C., Gologan, C., Pornet, C., Isikveren, A. T., and Hornung, M., "Battery Pack Modeling Methods for Universally-Electric Aircraft," 4th CEAS Air & Space Conference, Linköping, Sweden, September 16-19 2013.

[48] Patterson, M. D., and German, B. J., "Simplified Aerodynamics Models to Predict the Effects of Upstream Propellers on Wing Lift," 53rd AIAA Aerospace Sciences Meeting, Kissimmee, FL, USA, January 5-9 2015.

[49] Roskam, J., *Methods for estimating drag polars of subsonic airplanes*, Roskam Aviation and Engineering Corporation, 1971.

[50] Ting, L., Liu, C. H., and Kleinstein, G., "Interference of Wing and Multipropellers," *AIAA Journal*, Vol. 10(7), 1972, pp. 906–914.

[51] Biber, K., "Estimating Propeller Slipstream Drag on Airplane Performance," *Journal of Aircraft*, Vol. 48(6), 2011, pp. 2172–2174.

[52] Marcus, E. A. P., de Vries, R., Raju Kulkarni, A., and Veldhuis, L. L. M., "Aerodynamic Investigation of an Over-the-Wing Propeller for Distributed Propulsion," 2018 AIAA Aerospace Sciences Meeting, Kissimmee, FL, USA, January 8-12 2018.

[53] European Aviation Safety Agency, "Certification Specifications and Acceptable Means of Compliance for Large Aeroplanes," CS-25/Amendment 21, 2018.

[54] IHS, "Jane's All the World's Aircraft," , accessed May 2018. URL `https://janes.ihs.com`.

[55] Gerssen-Gondelach, S. J., and Faaij, A. P. C., "Performance of batteries for electric vehicles on short and longer term," *Journal of Power Sources*, Vol. 212, 2012, pp. 111–129.

[56] Stückl, S., "Methods for the Design and Evaluation of Future Aircraft Concepts Utilizing Electric Propulsion Systems," PhD Dissertation, Technische Universität München, 2016.

[57] Lents, C., Hardin, L., Rheaume, J., and Kohlman, L., "Parallel Hybrid Gas-Electric Geared Turbofan Engine Conceptual Design and Benefits Analysis," 52nd AIAA/SAE/ASEE Joint Propulsion Conference, Salt Lake City, UT, USA, July 25-27 2016.

Errata[‡‡]

Correction 1:
Equation 12 and the last sentence of Sec. II.A.2 are incorrect, and should be replaced by: “Finally, if the load factor n is specified as a requirement, this parameter can be related to the turn radius using $n = \sqrt{1 + (V^2/gR_{\text{turn}})^2}$.”

Correction 2:
The terms $(1 - \Phi)$ and $(1 - \varphi)$ of the coefficient matrix of Eq. 21 are incorrect. The equation should be expressed as:

$$\begin{bmatrix} -\eta_{\text{GT}} & 1 & 0 & 0 & 0 & 0 & 0 & 0 & 0 & 0 \\ 0 & -\eta_{\text{GB}} & 1 & 1 & 0 & 0 & 0 & 0 & 0 & 0 \\ 0 & 0 & 0 & -\eta_{\text{P1}} & 0 & 0 & 0 & 0 & 1 & 0 \\ 0 & 0 & -\eta_{\text{EM1}} & 0 & 1 & 0 & 0 & 0 & 0 & 0 \\ 0 & 0 & 0 & 0 & -\eta_{\text{PM}} & -\eta_{\text{PM}} & 1 & 0 & 0 & 0 \\ 0 & 0 & 0 & 0 & 0 & 0 & -\eta_{\text{EM2}} & 1 & 0 & 0 \\ 0 & 0 & 0 & 0 & 0 & 0 & 0 & -\eta_{\text{P2}} & 0 & 1 \\ \Phi & 0 & 0 & 0 & 0 & (\Phi - 1) & 0 & 0 & 0 & 0 \\ 0 & 0 & 0 & \varphi & 0 & 0 & 0 & (\varphi - 1) & 0 & 0 \\ 0 & 0 & 0 & 0 & 0 & 0 & 0 & 0 & 1 & 1 \end{bmatrix} \cdot \begin{bmatrix} P_{\text{f}} \\ P_{\text{gt}} \\ P_{\text{gb}} \\ P_{\text{s1}} \\ P_{\text{e1}} \\ P_{\text{bat}} \\ P_{\text{e2}} \\ P_{\text{s2}} \\ P_{\text{p1}} \\ P_{\text{p2}} \end{bmatrix} = \begin{bmatrix} 0 \\ 0 \\ 0 \\ 0 \\ 0 \\ 0 \\ 0 \\ 0 \\ 0 \\ P_{\text{p}} \end{bmatrix} \tag{21}$$

Correction 3:
The symbol used for the fraction of wingspan occupied by the DP array in Fig. 8 should be $(\Delta y/b)$ instead of $\tilde{b}_{\text{dp}}$, as indicated below:

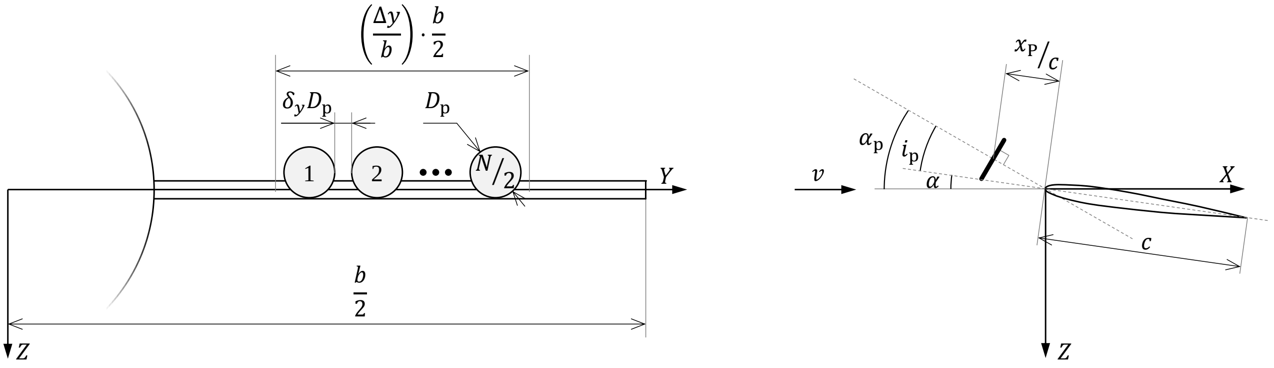

Fig. 8 Simplified DP-system representation, indicating the main geometrical parameters.

Correction 4:
Equation 30 should be expressed as:

$$a_{\text{P}} = \frac{\Delta v_{\text{p}}}{v} = \frac{1}{2}\left(\sqrt{1 + \frac{8}{\pi \rho v^2} \frac{\left(T_{\text{p}}/W\right)}{\left(D_{\text{p}}^2/W\right)}} - 1\right) \tag{30}$$

[‡‡] This list of errata is not included in the version of this document published on https://arc.aiaa.org/, but can be accessed using the Crossmark update.

Correction 5:
The induction factor a used in Eq. 33 should contain a subscript “p”, i.e.:

$$\frac{R_{c/4}}{R_{\mathrm{p}}} = \sqrt{\frac{1 + a_{\mathrm{p}}}{1 + a_{\mathrm{p}}\left(1 + \frac{x'_{\mathrm{p}}/R_{\mathrm{p}}}{\sqrt{\left(x'_{\mathrm{p}}/R_{\mathrm{p}}\right)^2 + 1}}\right)}}. \tag{33}$$

Correction 6:
Equation 34 should be expressed as:

$$a_{c/4} = \frac{1 + a_{\mathrm{p}}}{\left(R_{c/4}/R_{\mathrm{p}}\right)^2} - 1. \tag{34}$$

Correction 7:
The span-fraction occupied by the DP array should multiply the sectional coefficients of Eqs. 40a-40c, such that:

$$\Delta C_L = \Delta c_l \left(\frac{\Delta y}{b}\right) \tag{40a}$$

$$\Delta C_{D_0} = \Delta c_{d_0} \left(\frac{\Delta y}{b}\right) \tag{40b}$$

$$\Delta C_{D_i} = \Delta c_{d_i} \left(\frac{\Delta y}{b}\right) \tag{40c}$$